Monitoring and Mapping Floodplain Understorey and Short-Vegetation Evapotranspiration

Huade Guan, Wenjie Liu, Robin Keegan-Treloar, Karina Gutierrez-Jurado, David Bruce, Jianfeng Gou, Robert Keane, Lawrence Burk, Okke Batelaan

National Centre for Groundwater Research and Training,

College of Science and Engineering, Flinders University, Australia

and

Jessica Thompson

Murry-Darling Basin Authority, Australia
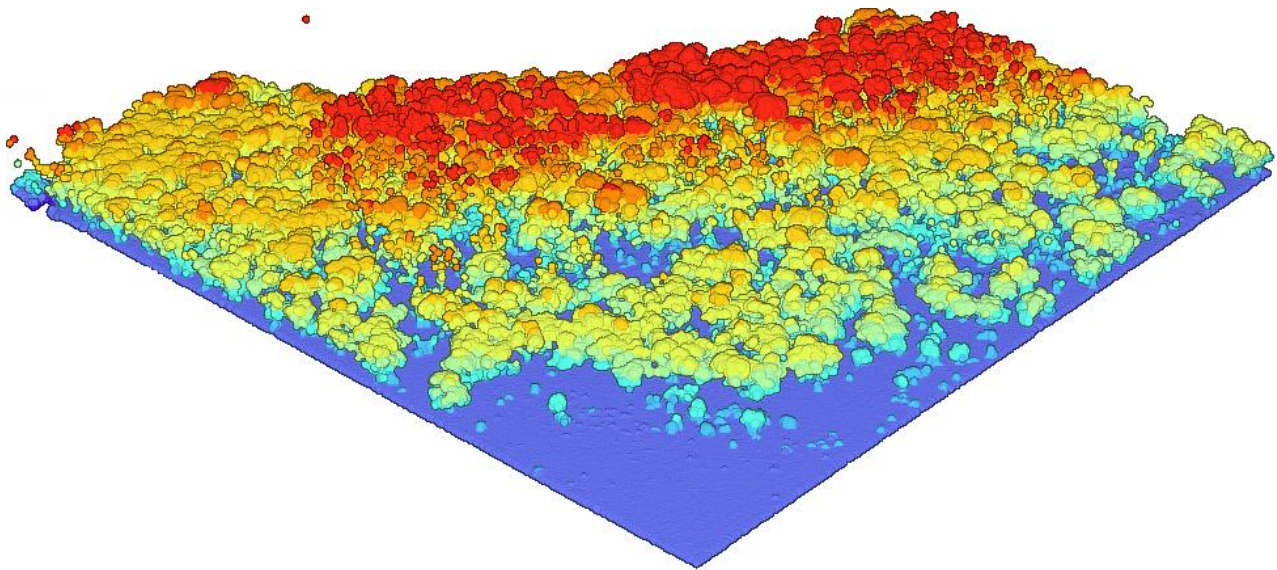
5 March 2024

Acknowledgement

Executive Summary

Understorey evapotranspiration (ET) is an important unknown in the water balance of the Murray-Darling Basin. This study adapted a novel method, i.e., Maximum Entropy Production (MEP) ET modelling, for monitoring and mapping ET from floodplain woodland understorey and short-vegetation surfaces. The understorey in a River Red Gum (RRG) woodland was investigated, together with two surfaces covered by Lignum shrubs and Subshrub bushes. The project was running from spring 2021 to spring 2023 with the objective to quantify temporal and spatial variation of understorey and short-vegetation ET in three sections of a floodplain with different vegetation cover. During the project, the 2022-2023 River Murray flood occurred, providing a unique opportunity to examine how ET from the understorey and short-vegetation areas responded to the flooding. The investigation was based on continuous micrometeorological data collection at three stations and about 30 iButton (measuring temperature and humidity) locations, and 11 drone thermal imagery surveys over three sections of an in total 100 hectare (ha), Murray River floodplain, near Lock 4, Bookpurnong, South Australia.

The results indicate that the RRG understorey lost on average 214 mm of water by ET in one year (November 2021-October 2022), while the Subshrub surface lost 288 mm, and the Lignum surface lost 365 mm. Their mean 2.14, 2.88, and 3.65 ML per hectare water loss per year is solely due to evapotranspiration from the three surfaces, respectively. Over the same period, the accumulated precipitation was 3.12 ML per hectare in the area. These results imply that ET significantly varies among woodland understorey and short-vegetation surfaces.

The response to the 2022-2023 River Murray flood varied among three areas. The Lignum site experienced a significant increase in ET, peaking 40% higher than the previous year, likely due to Lignum shrub regrowth after the flood. The Subshrub site's ET rates also increased, reaching a peak in July, likely influenced by increased soil moisture from both rainfall and antecedent floodwater infiltration. At the RRG understorey, the flood did not cause observable ET changes, likely due to sandy soil texture and a shallow herbaceous understorey root zone.

The mapping results suggest that the RRG understorey has a larger spatial variability of ET than the Subshrub and Lignum areas. One MEP station is probably not sufficient to obtain representative ET estimation for the whole understorey. We recommend the use of the spatial modelling methods

developed in this project, aided with an ambient weather station, regular drone thermal surveys, once per season LiDAR surveys, and distributed relative humidity and temperature monitoring points.

Table of Contents

List of Figures

List of Tables

1 Introduction

Evapotranspiration (ET) from woodland and forest understorey can be significant. A recent review of boreal and temperate forests suggests understorey ET can contribute to over 50% of the total ET when overstorey leaf area index (LAI) is below one, and to around 25% when the overstorey LAI is above three (*Balandier et al.,* 2022).

Understorey ET is an important unknown in the water balance equation of the Murray-Darling Basin. While tree transpiration has been monitored at a number of floodplain sites, evapotranspiration rates from the woodland/forest understorey and from the area covered by short vegetation are the next unknowns to be investigated in the floodplain environment. This project aims to monitor and map ET for woodland understorey and areas with short vegetation cover.

Vegetation cover varies over short distances on floodplains due to spatial variation of soil properties, salinity, topographic relief, and depth to groundwater. In addition to transpiration, soil evaporation can be significant in floodplains. Since salinity influences evaporation and transpiration differently, spatial variability of soil salinity complicates the estimation of floodplain ET. In River Murray floodplains, episodic operations of the salt interception schemes create localised groundwater drawdown, which adds another factor to the complexity of floodplain ET estimation. In such an environment, a reliable and small-footprint method is required to measure and map spatially variable ET.

The objectives of this project are to (1) adapt and apply a novel ET method (Maximum Entropy Production (MEP) – ET) to monitor understorey, and short-vegetation surface ET in a floodplain environment; (2) develop an ET upscaling approach based on temporally continuous data monitoring at selected locations and spatially continuous drone images at selected time points; (3) estimate daily, monthly, and annual floodplain water loss through understorey and short-vegetation surface ET over the study period; and (4) improve our understanding of understorey and short-vegetation surface ET processes. The project encountered the 2022-23 River Murray flood, the third highest flood ever recorded in South Australia. The flood provided a unique opportunity to (5) investigate how the understorey ET responds to flooding events.

This report summarises the methodology development, field investigations, drone observations, data analyses, ET modelling and mapping, over three sections of the floodplain with different vegetation covers.

2 Methodology

2.1 Study sites and instrumentation

The study sites are located in Clark's floodplain in Bookpurnong along the eastern bank of the River Murray in South Australia. The three sites are covered by (1) a *Eucalyptus camaldulensis* (common name: River Red Gum (RRG)) woodland understorey; (2) *Muehlenbeckia florulenta* (Lignum); and (3) small bushes *Sclerolaena sp.* (Bindyi) and *Atriplex sp.* (Saltbush) and are respectively referred to as the RRG understorey site, the Lignum site, and the Subshrub site. The RRG understorey includes woody vegetation, short herbaceous plants, and bare soil. ET estimation for the herbaceous plants and bare soil surface is the focus for the RRG understorey site. In addition, a nearby *Eucalyptus largiflorens* (Black Box) understorey is also monitored for temperature and humidity.

Three MEP monitoring stations and about thirty temperature and humidity sensors (iButtons) are installed over the four vegetation areas in the floodplain (Figure 1).

Figure 1 Distribution of field equipment in Clark's floodplain, south of Berri, showing the MEP stations at RRG woodland understorey, Subshrub, and Lignum site. 30 humidity and temperature sensors are spread over the three sites and a Black Box woodland understorey site.

The MEP stations for the RRG woodland understorey and the Subshrub were installed in August 2021. Each station consisted of a net radiometer, a thermal infrared radiometer, and a sensor measuring air temperature and relative humidity. The equipment setup is shown in Figure 2.

The third station at the Lignum site was installed in October 2021, due to a COVID-related delay in the equipment supply. This station was equipped with a four-component radiometer, a net radiometer, a

thermal infrared radiometer, four pairs of air temperature and relative humidity sensors, and two heat plates for measuring ground heat flux (Figure 3).

The three MEP stations provided half-hourly data on net radiation, relative humidity, and air temperature for the MEP-ET models. The thermal infrared radiometer provides additional information on surface temperature and inference of plant water stress conditions where applicable. The four-component radiometer installed at the Lignum site provides downwelling shortwave radiation for radiation modelling across the floodplain.

Two sets of air temperature and relative humidity at two levels, installed at the Lignum and Subshrub sites for a short period, provide measurements for ET estimation based on the Bowen ratio energy balance method, which provides independent ET estimates from what the MEP-ET model calculates.
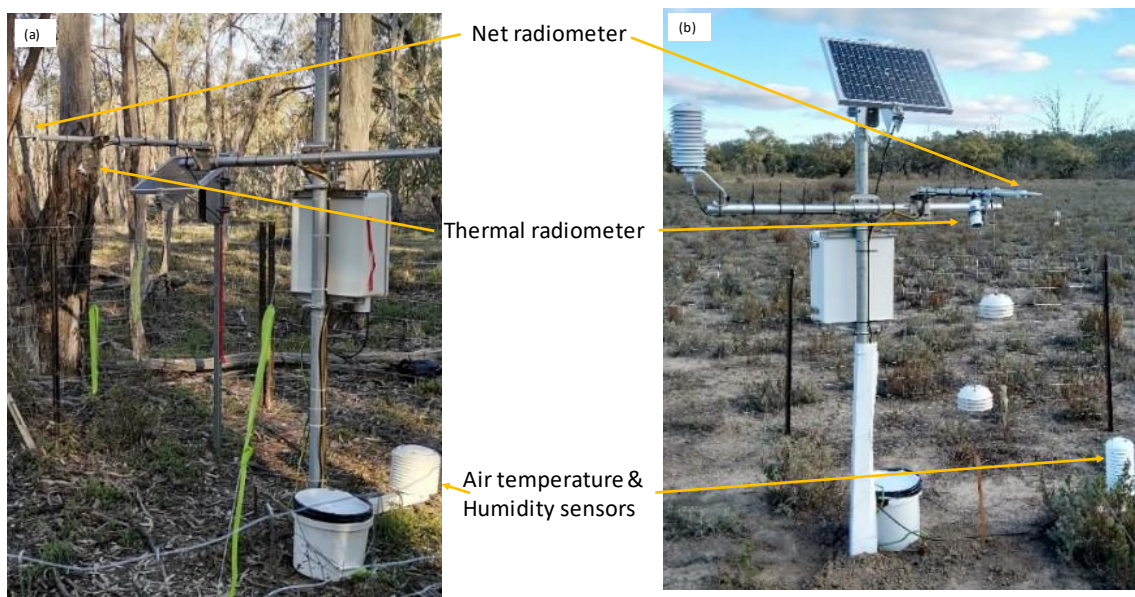
Figure 2 The MEP stations at the (a) RRG woodland understorey site; and (b) Subshrub site.
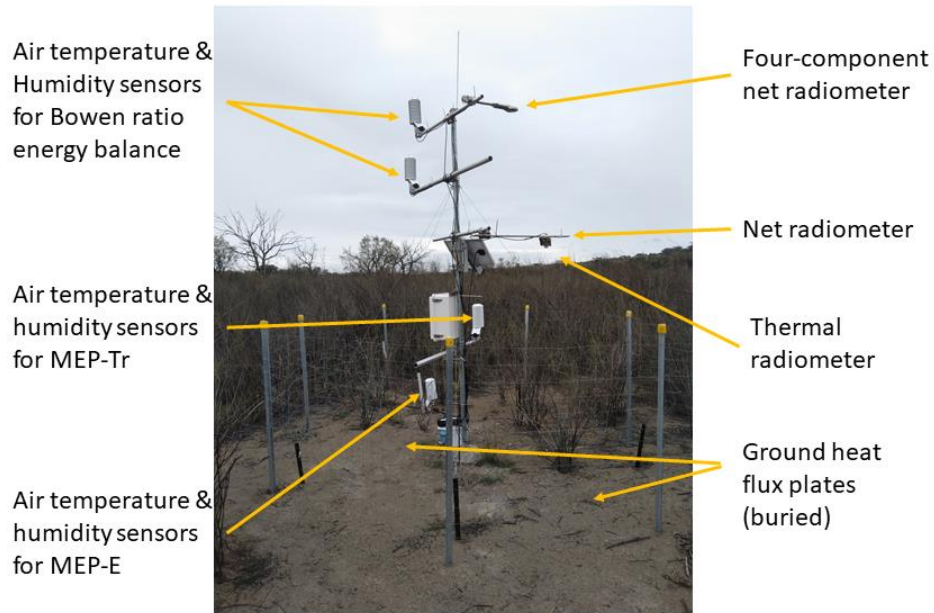
Figure 3 The equipment setup at the Lignum site, including measurements required for MEP modelling of evaporation from the ground and transpiration from the vegetation canopy, and measurements for the Bowen ratio energy balance estimation of ET of the Lignum-covered area.
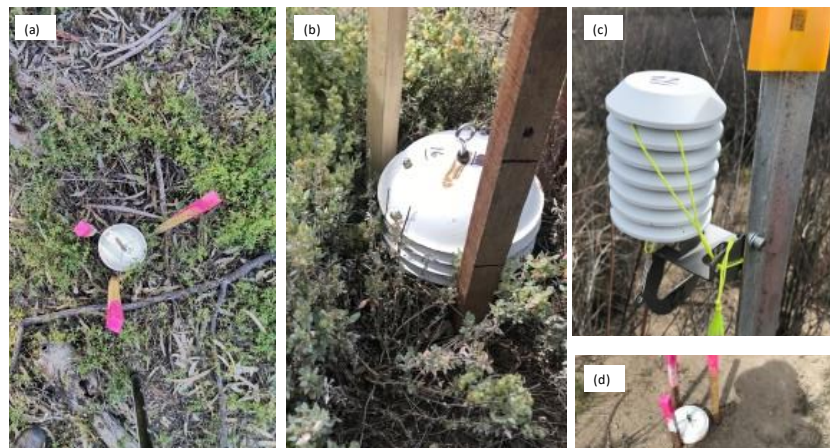
Figure 4 Photos (from left to right) showing the temperature and humidity sensors installed at (a) the RRG understorey site; (b) the Subshrub site; and at (c)-(d) two levels at the Lignum site.

2.2 Drone Observations

An Unpiloted Aerial Vehicle (UAV) or drone was used to capture thermal infrared images over three portions of the floodplain representative of the RRG, the Subshrub, and the Lignum areas. A light detection and ranging (LiDAR) survey was undertaken over the three vegetated areas of the floodplain for derivation of ground and vegetation height, and overstorey leaf area index. A DJI Matrice 300RTK drone (Figure 5) was used as the flying platform. The drone incorporated a Global Navigation Satellite System (GNSS) receiver and antennae, and Inertial Navigation Unit (INU) sensors for position and orientation, respectively.

The thermal infrared sensor, a DJI Zenmuse H20T 640 measures over the wavelength range of 8 -14 μm in a single band, collecting images of emitted thermal radiation. Real Time Kinematic (RTK) position and orientation from the drone enabled accurate 3D positioning of each image. Higher spatial resolution images were simultaneously captured from a 20 mega-pixel RGB camera with the thermal image collection. Different flight heights were utilised to experiment with mosaicking the thermal images to create a single-temperature mosaic. For Lignum and Subshrub areas, the flight height was set to 60 m above ground and the corresponding thermal image resolution is ~5 cm. For RRG area, the flight height was set to 40 m for higher spatial resolution (~3 cm) thermal imagery.

Temperature captured by the thermal camera reflects the spectral thermal energy emitted by the surface target pixel through the air column between the pixel and the camera. The ambient humidity and temperature measured at corresponding stations was applied to correct for the air column effect. The emissivity of sensed objects was assumed to be 0.95. This correction process was carried out using the DJI Thermal SDK package (https://www.dji.com/downloads/softwares/dji-thermal-sdk). The image mosaic was performed use the Pix4D mapper software following the established workflow for thermal camera imagery.

Figure 6 compares the temperature estimated from the drone thermal images and that from the station thermal sensors for the Lignum and Subshrub sites over the whole project period. The results show good consistency between the two sets of measurements.
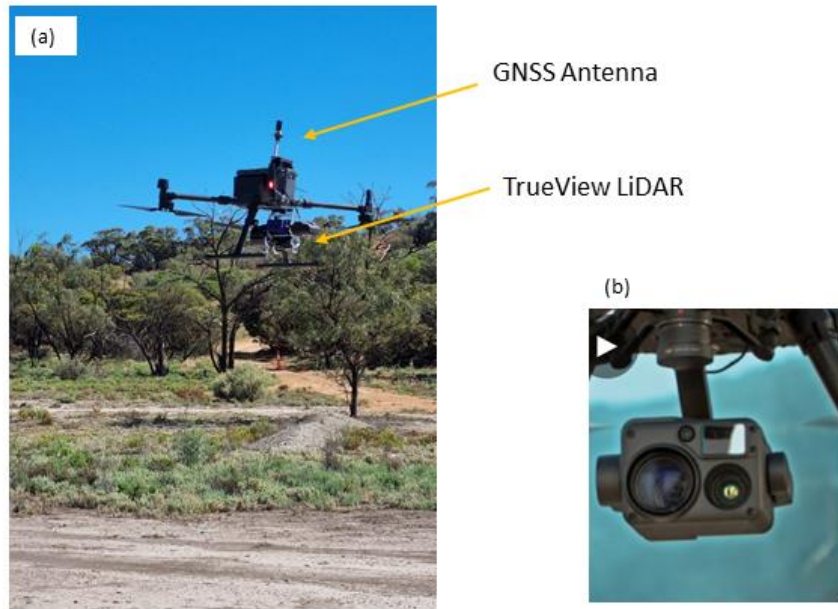
Figure 5 (a) DJI Matrice 300 RTK drone with TrueView 410 LiDAR; (b) Zenmuse H20T Thermal camera.
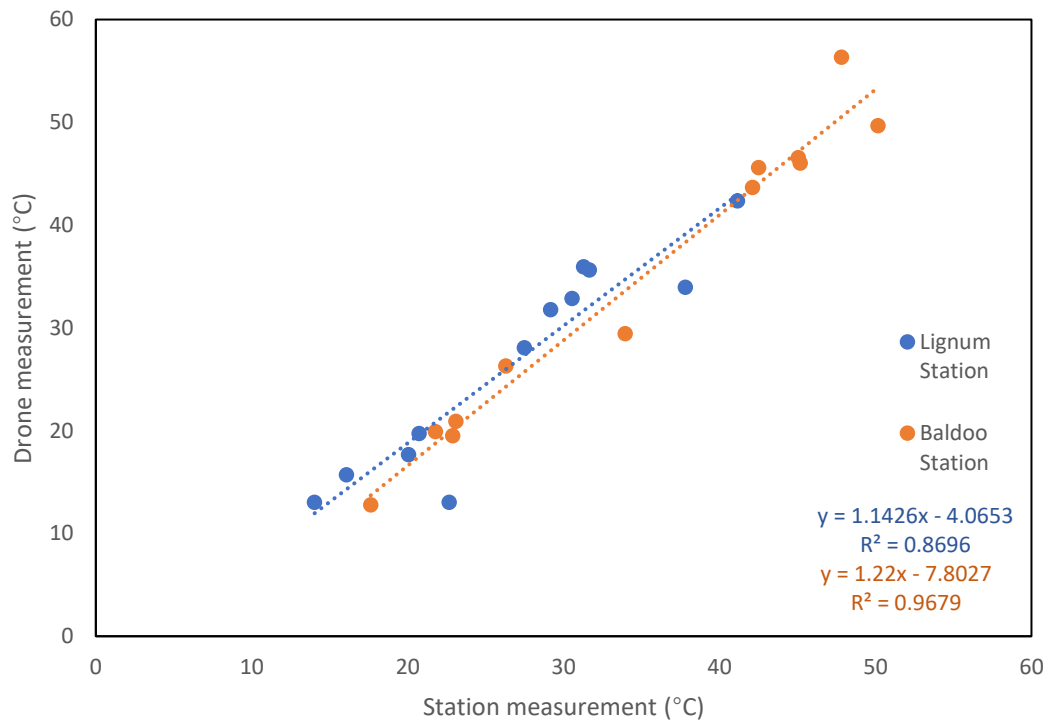
Figure 6 Scatter plots of surface temperatures measured at the stations and measured from the drone thermal images for the Lignum and Subshrub sites over the whole project period.

The 3D observations of ground objects were obtained from a TrueView 410 3DIS LiDAR. This system uses 8 laser beams to produce 420,000 laser pulses per second and records three laser returns per pulse (precision: ~20 mm on one strip, accuracy: ~30 mm). Simultaneously, two 20 mega-pixel cameras record RGB imagery so that each point in the subsequently generated 3D point cloud can be colourised. The LiDAR sensor has its own GNSS and INU units to record the position and orientation of each laser pulse.

In this project, instead of using the GNSS embedded in the Drone, a GNSS ground station was set up prior to and through the course of LiDAR capture. This ground station recorded the differential GNSS corrections to be applied to the 3D position of every LiDAR pulse and thus involved post-processing of data and enabled actual, rather than predicted, GNSS satellite orbits to be used, thus improving the quality of the positioning. The LiDAR data was processed in EVO software (a very close relative to LP360) and generated very large 3D point clouds, including positions of ground and above-ground features (grass, shrubs, branches, leaves in trees, and canopy surface). The image on the front page of this report shows a perspective view of a 3D point cloud over the RRG woodland, which has been colourised by height.

The average point density across the entire area was 459 points/m^2, while within the RRG vegetation-covered area, the density reached 607 points/m^2. Such high point densities are crucial for accurately representing canopy structures. We recommend a point density of at least 500 points/m^2 for generating LAI at a one-meter scale.

2.3 LAI measurements

LAI describes the density of vegetation canopy cover. It is a dimensionless quantity defined as the one-side green leaf area over the unit ground surface. In this project, we estimate the LAI from LiDAR measurements and calibrate it with in-situ observations using an AccuPAR PAR/LAI Ceptometer (Model LP-80).

LAI can be estimated from the LiDAR data, based on the Beer-Lambert law (*Wang and Fang*, 2020):

$$LAI = -\frac{1}{k}\ln(N_{ground}/N_{total}) \tag{1}$$

where N_{ground} is the number of return LiDAR points from the ground level, N_{total} is the total number of the return LiDAR points, and k is the extinction coefficient. The k value is calibrated based on field observation. Empirically, a threshold distance above ground can be used to classify LiDAR points into ground and above-ground points. In this project, the reference ground points were automatically identified in ArcGIS Pro software. Based on our preliminary test, a threshold distance of 0.3 m was applied to classify the LiDAR points into ground and above-ground points. This particular threshold was determined through a visual inspection of the smoothness of classified ground points at various height settings.

Field observations of LAI were used to calibrate the LiDAR estimations. The AccuPAR sensor measures the Photosynthetically Active Radiation (PAR) above and under the canopy and calculates the LAI based on the following equation (the AccuPAR LAI Ceptometer manual, https://publications.metergroup.com/Manuals/20442_LP-80_Manual_Web.pdf):

$$LAI = \frac{\left[\left(1 - \frac{1}{2K}\right)f_b - 1\right]\ln\tau}{A(1 - 0.47f_b)} \tag{2}$$

where K is the extinction coefficient for the canopy, f_b is the incident beam PAR fraction, τ is the ratio of the PAR measured below the canopy to the PAR above the canopy. $A = 0.283 + 0.785a - 0.159a^2$ (a is the leaf absorptivity in the PAR band, assumed to be 0.9).

2.4 The maximum entropy production method

Although the commonly used eddy covariance method can be applied in an understorey environment under some circumstances (*Lamaud et al.*, 2001), it has not been commonly used to monitor understorey ET. This is partly because sensible heat storage in the understorey space and its dynamics increase the complexity of using the method. Another limitation of using the eddy covariance method comes from the size of the homogeneous surface, which is often too small to meet the fetch criteria for the method. The same problems apply to the Bowen ratio energy balance method (*Heilman et al.*, 1989).

Here we apply a new surface energy partitioning method – Maximum Entropy Production (*Wang and Bras*, 2009; *Wang and Bras*, 2011). The MEP method is different from conventional physically based

methods. It is derived from the maximum entropy theory for the nonequilibrium thermodynamic systems. The MEP method partitions net radiation energy on a surface into sensible heat flux, latent heat flux, and ground heat flux (*Wang and Bras*, 2011), based on temperature and specific humidity measured at the surface at a regular time intervals (e.g., 30 minutes).

The MEP method requires a much smaller set of data than the eddy covariance method, which needs high frequency (e.g., 10 Hz) three-dimensional wind velocity, temperature, and specific humidity data. It is also simpler than the Bowen ratio energy balance method, which requires a long fetch and more data, including ground heat flux, temperature and humidity at two levels.

Another characteristic of the MEP method is its small footprint of a few meters. Thus, it does not require a fetch as large as hundreds of meters as is required for the eddy covariance and Bowen ratio energy balance methods. These characteristics make the MEP method a perfect method to monitor ET in the floodplain environment.

As mentioned above, the MEP method only requires three variables, net radiation (R_n), air temperature (T_a) and specific humidity (q_s) close to the surface from which evaporation or transpiration is to be estimated. The air temperature close to the evaporating surface results from the sensible heat flux, while the humidity results from the latent heat flux. These variables are required to construct the "dissipation function" or "entropy production function" (*Wang and Bras*, 2009), which is then solved for the extremum using the Lagrange multiplier method.

2.4.1 The MEP-Evaporation model

The mathematical derivation (Wang and Bras, 2011) of the MEP-Evaporation model results in the following equations (Equations 3-7).

$$E + H + G = R_n \tag{3}$$

where *E* is the latent heat flux, *H* is the sensible heat flux, *G* is the ground heat flux.

$$E = B(\sigma)H \tag{4}$$

$B(\sigma)$ is the reciprocal of the Bowen ratio, which can be calculated from σ.

17

$$B(\sigma) = 6\left(\sqrt{1 + \frac{11}{36}\sigma} - 1\right) \tag{5}$$

$$\sigma = \left(\frac{\lambda^2}{c_p R_v} \frac{q_s}{T_s^2}\right) \tag{6}$$

$$G = \frac{B(\sigma)}{\sigma} \frac{I_s}{I_o} H|H|^{-\frac{1}{6}} \tag{7}$$

where σ is a function of specific humidity and air temperature close to the evaporating surface, λ is the latent heat of vaporisation based on surface temperature, c_p is the heat capacity of air, R_v is ideal gas constant divided by the molecular mass of water vapour, I_s and I_o are the inertia terms in defining the entropy production from sensible heat flux and ground heat flux, respectively.

In this project, we applied MEP-Evaporation for the RRG woodland understorey and the Subshrub surface because the vegetation is within 30 cm of the ground surface. The measured specific humidity near the ground surface (10-30 cm) captures the effect of both soil evaporation and short vegetation transpiration at both sites.

2.4.2 The MEP-Transpiration model

The MEP-Transpiration model (*Wang and Bras,* 2011) is formulated by Equation 8 and 9:

$$E_c = \frac{R_{nc}}{1 + B^{-1}(\sigma)} \tag{8}$$

$$H = \frac{R_{nc}}{1 + B(\sigma)} \tag{9}$$

where E_c is the transpiration, R_{nc} is the partitioned net radiation for transpiration, other symbols are as explained earlier.

At the Lignum site, we applied the MEP-Transpiration model to simulate Lignum canopy transpiration and the MEP-Evaporation model to simulate lignum understorey (mostly bare soil) evaporation. To

honour the energy balance in the MEP ET calculation, it is necessary to partition the net radiation between the vegetation surface and the ground surface.

$$R_{nc} = X_c R_n \tag{10}$$

where X_c is the fraction of net radiation absorbed by the canopy. For a partially vegetated surface like the Lignum site, the vegetation canopy intercepts more solar radiation when the solar angle is low. Here we consider the solar angle effect on the instantaneous net radiation partitioning.

$$X_c = 1 - (1 - F) * \sin \varepsilon \tag{11}$$

where F is the fractional vegetation cover, and ε is the instantaneous solar elevation angle. For the lignum site, we assume F = 0.5. During the nighttime there is no solar radiation and X_c is assumed to be 0.5.

The Lignum shrubs are about 1.5 meters high. In this floodplain environment, measurement of air temperature and humidity at this height may be "contaminated" by the ambient air (e.g., from the nearby river and ponds), which is not representative of the Lignum shrubs. Thus, some correction is required (*Gutierrez-Jurado et al.*, 2015; *Hajji et al.*, 2018). Here, we applied a stress factor in the σ function, which is a novel contribution to the method. We adopted a method similar to (*Liu et al.*, 2020), in which air and canopy temperature differences are applied to estimate the water stress for the Lignum MEP-transpiration modelling.

The stress factor is

$$\text{SI} = \frac{\Delta T - \Delta T_{wet}}{\Delta T_{dry} - \Delta T_{wet}} \tag{12}$$

ΔT is the daily maximum difference between the canopy and air temperatures, ΔT_{wet} is the minimum of the ΔT time series and ΔT_{dry} is the maximum of the ΔT timeseries.

This stress factor is then incorporated into the σ function (*Hajji et al.*, 2018) as follows.

$$\sigma = \left(\frac{\lambda^2}{c_p R_v} \frac{q_s}{T_s^2}\right)(1 - SI) \tag{13}$$

The MEP ET simulations were programmed in Python. The MEP-Evaporation functions were solved iteratively by first setting $H^{(1)} = \frac{R_n}{2}$ then iteratively updating the H estimate using the equation provided by Jingfeng Wang from Georgia Institute of Technology, USA:

$$H^{(k+1)} = \frac{R_n |H^k|^{\frac{1}{6}}}{\frac{B(\sigma) I_s}{\sigma I_0} + (1 + B(\sigma))|H^k|^{\frac{1}{6}}} \quad k = 1, 2, 3 \tag{14}$$

We set a convergence criterium of $1E^{-6}$ Wm^{-2} (i.e., the change in H values between iterations at which to terminate the model), which was generally met within 6-8 iterations.

2.5 The Bowen ratio energy balance method

For the Lignum and Subshrub sites, a reasonable fetch is available for the Bowen ratio energy balance (BREB) method. We added two levels of air temperature and humidity measurements so that the BREB method can be applied to produce independent ET estimation concurrent with the MEP ET estimation. At the Lignum site, we also installed two ground heat flux plates. While for the Subshrub site, no ground heat flux was measured. We used MEP estimated ground heat flux for the BREB method.

The BREB method is defined by

$$E = \frac{R_n - G}{1 + \beta} \tag{15}$$

$$\beta = \gamma \frac{T_1 - T_2}{e_1 - e_2} \tag{16}$$

Where β is the Bowen ratio, T and e are air temperature and vapor pressure measured at two vertical levels, γ is the psychrometric constant.

2.6 Radiation modelling

To obtain the net radiation of the understorey surface, we simulate the downwelling shortwave radiation and convert the shortwave radiation to net radiation (Equation 18 in 2.9.1). A double-shading transposition (DST) model is employed to estimate the downwelling shortwave radiation for its capacity in simulating the radiation distribution under vegetation cover (*Liu et al.*, 2022). The model requires the following data: (1) time and location information; (2) topography and vegetation data, including digital terrain model (DTM), digital surface model (DSM), and leaf area index (LAI); and (3) reference radiation on a horizontal surface, free of shading effects, which shares the same sky condition with the area of interest with solar radiation to be simulated. These data were collected using the methods described in the previous sections. A flowchart for the DST model is shown in Figure 7.
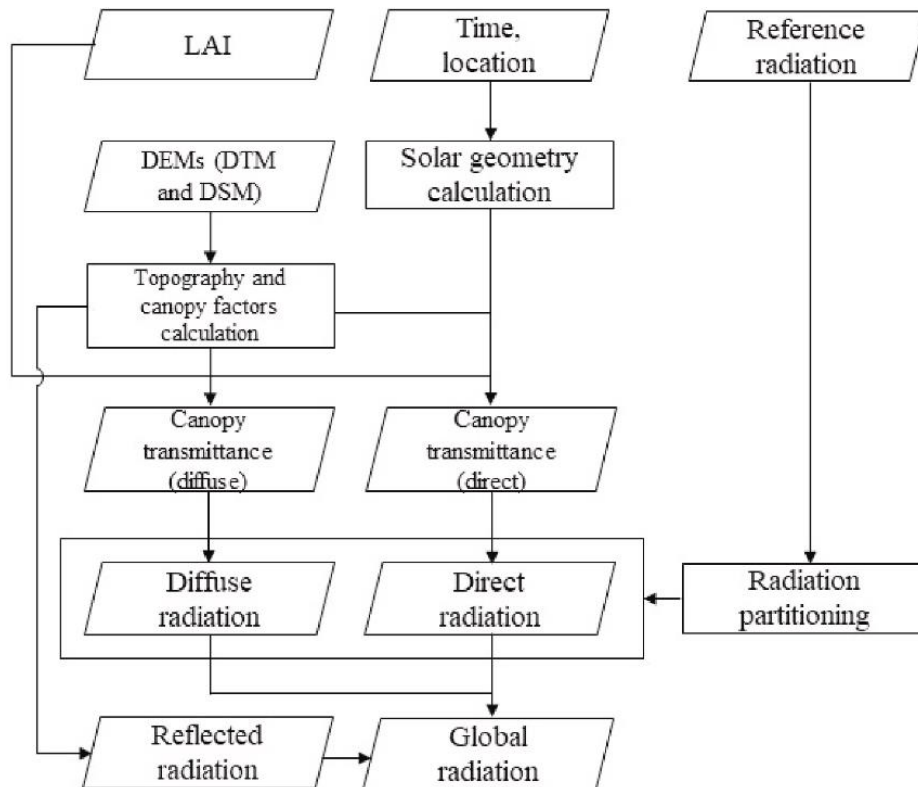
Figure 7 The double-shading transposition (DST) model flowchart.

2.7 Specific humidity modelling

Specific humidity refers to the ratio of the mass of water vapor to the total mass of moist air. Surface specific humidity (about ~10 cm above the soil surface) is an important variable reflecting moisture status at the interface of the atmosphere and the Earth's surface and a necessary input in the MEP method for ET estimation.

Here, we develop a method for predicting the deviation of surface specific humidity (q_s) from the ambient specific humidity (q_a) by using surface radiative temperature and ambient micrometeorological variables. A stepwise linear regression (SLR) method was adopted to build a multiple linear regression model by iteratively adding or removing independent variables from a set of candidate variables:

$$y = \beta_0 + \sum_{i=1}^{i=n} (\beta_i x_i) + \epsilon \tag{17}$$

where y is the dependent variable, β_i is the regression coefficient of the independent variable x_i, n is the number of the independent variables, and ϵ is the residual error.

Since surface specific humidity is highly correlated with ambient specific humidity data, which is readily available, it is more meaningful to estimate the deviation between the two. The surface specific humidity deviation (q_s-q_a) is selected as the dependent variable. The candidate variables comprise various meteorological factors grouped into three categories: current meteorological variables (ambient relative humidity, ambient temperature, radiative temperature, temperature difference between radiative temperature and ambient temperature, and net radiation), antecedent meteorological variables (including meteorological variables from the preceding time of the day and differences between the current and preceding moment's meteorological variables), and precipitation variables (daily precipitation and accumulated precipitation over 2, 3, 4, and 5 days, respectively). The significant level of the F-value for determining adding or removing independent variables is set at 0.05, and the Nash-Sutcliffe efficiency coefficient (NSE) is used to evaluate the model performance.

The entire sequence of data for each site is applied to determine the best prediction outcome at a particular time of the day. 80 % of data were randomly selected to build the multiple linear regression model, and the remaining 20 % were used to validate the model. The dominant analysis was adopted to

explore the specific contribution of different explanatory variables to the variance of the dependent variable.

A time-window of 3 months centred on each month of the entire study period is considered to determine the seasonal variation of predicted specific humidity difference. No cross-validation is conducted, considering the relatively small amount of data in 3 months.

2.8 Understorey surface temperature mapping

In addition to the net radiation distribution in the understorey (described in 2.6), the MEP-Evaporation model requires the distribution of surface temperature and specific humidity. The drone observation of surface temperature is a mix of canopy temperatures and understorey surface temperatures. It does not observe a spatially continuous distribution of understorey surface temperatures. Another novel methodology contribution is required in this project to produce the understorey temperature maps.

Firstly, a drone thermal image is categorised into two groups of pixels, one for the overstorey canopy temperatures and the other for the understorey temperatures. Each group covers only part of the total surface area. A LiDAR image is adopted to separate the two groups. We assume the area covered by tree canopy has a larger difference between LiDAR derived DSM and DTM (i.e., a larger Canopy Height Model (CHM)). After some trials, we select a threshold of 5 m to determine the area free of tree canopy cover (hereafter referred to as the open area). Figure 8 illustrates the open area derived from the LiDAR data captured on 4 March 2022.
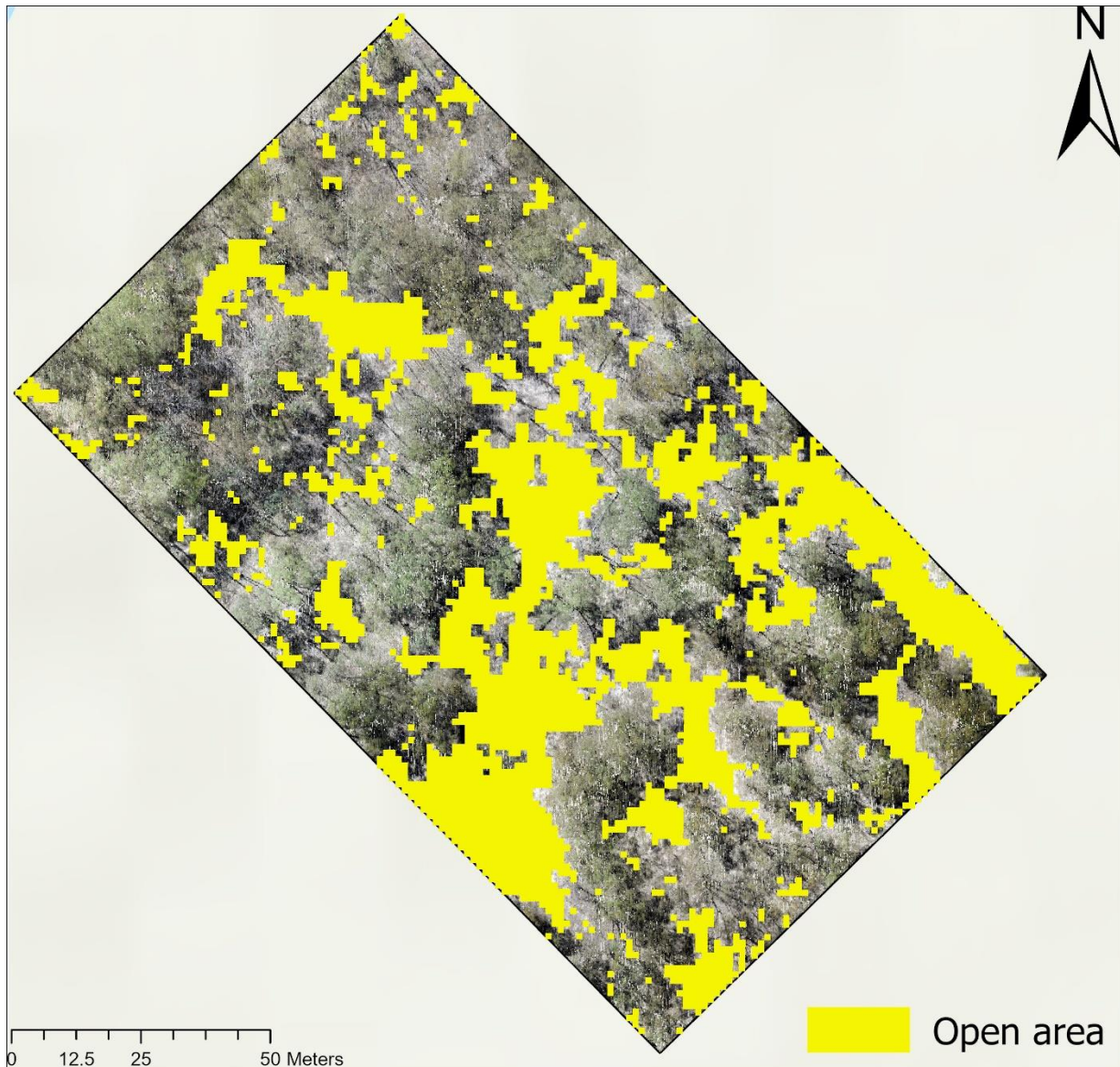
Figure 8 The open area (yellow colour) delineated based on LiDAR derived Canopy Height Model overlain by LiDAR RGB image captured on 4 March 2022.

By overlying the LAI image and the surface temperature image of the open area, a boxplot can be created (Figure 9). This plot reveals a trend where an increase in LAI is associated with a decrease in surface radiative temperature, along with reduced variability. The lower boundary of the boxplot very likely represents the canopy temperature, which remains consistent regardless of LAI conditions. We assume the mean values (the orange dots) are the typical understorey temperature for different LAI conditions. We are then to find the relationship between collocated understorey temperature and LAI.

24

Figure 10 displays the application of this method at four drone survey times. In Figure 10(a), the LiDAR and thermal data were collected two days apart. In Figures 10(b), 10(c), and 10(d), the thermal images were taken 1, 2, and 3 months, respectively, after the LiDAR survey. The R-squared values progressively decrease as the time interval between the thermal imaging and the LiDAR survey increases. Therefore, for establishing a more robust and accurate relationship, it is recommended to conduct the LiDAR and thermal surveys as close in time to each other as possible.
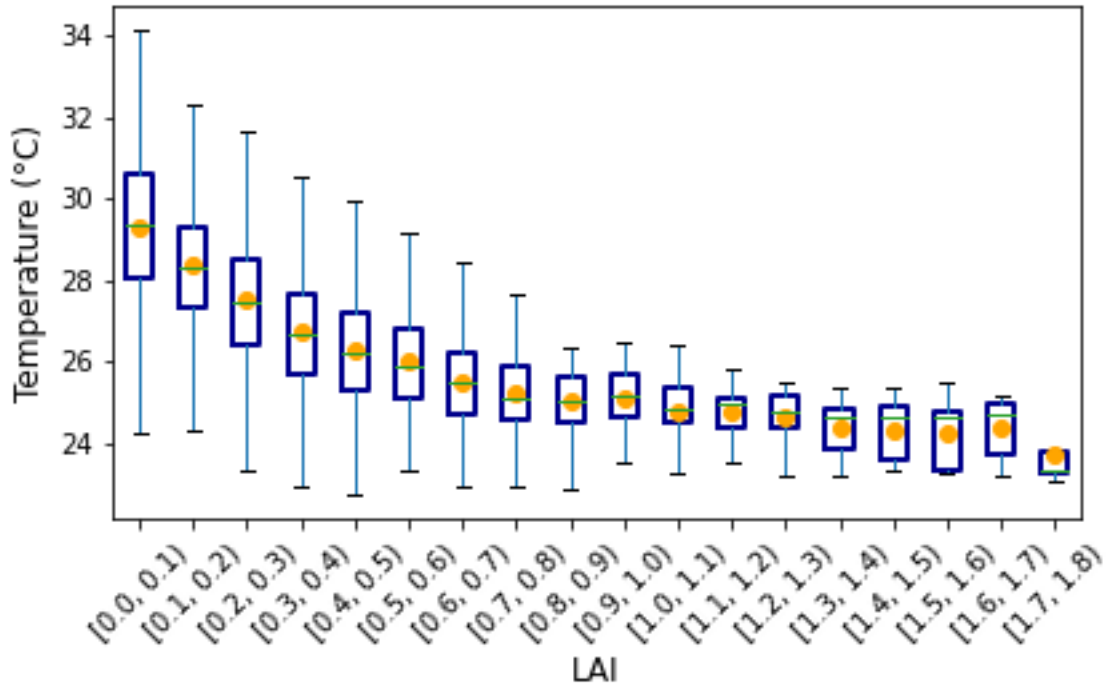
Figure 9 Boxplot of LiDAR (captured on 04/03/2022) derived LAI and surface temperature from a drone survey (captured on 04/03/2022). Orange dots are the mean value of each box.
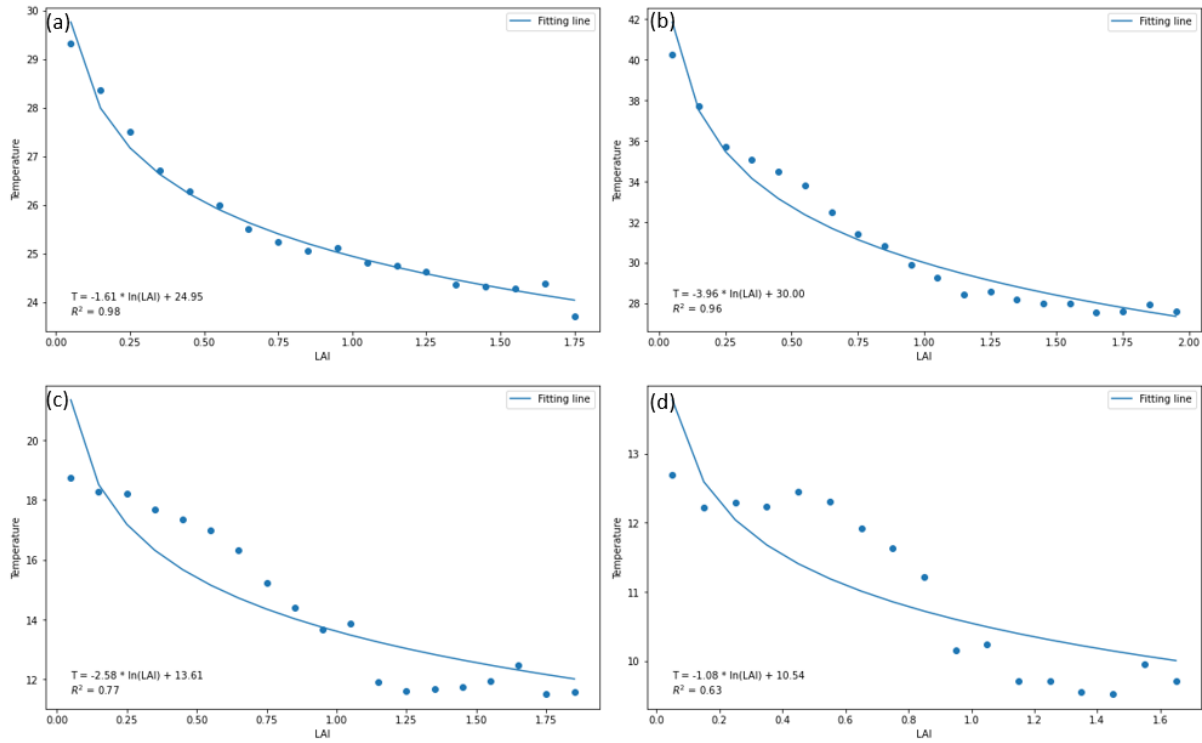
Figure 10 Logarithmic regression of understorey surface radiative temperature and mean LAI (interval = 0.1). The thermal images from (a)-(d) were captured on 04/03/2022, 10/04/2022, 07/05/2022, and 25/06/2022, respectively.

2.9 Instantaneous and daily ET mapping

Instantaneous understorey ET mapping is produced for drone thermal image capture times based on the MEP-Evaporation model. This means that the relevant net radiation mapping and specific humidity mapping should be done at the same time. Once the instantaneous understorey ET maps are produced for all cases when thermal images are available, they are upscaled to daily ET maps and monthly ET maps based on the diurnal and seasonal variation of understorey ET patterns from the relevant MEP stations.

2.9.1 Instantaneous ET mapping

We apply the MEP ET models to produce instantaneous ET maps for three surfaces with monitoring stations. The instantaneous net radiation is calculated based on

$$R_n = (1 - \alpha_{surf})R_s \downarrow + \varepsilon_{surf}\varepsilon_{atm\_adj}\sigma T_a^4 - \varepsilon_{surf}\sigma T_s^4 \tag{18}$$

26

where α_{surf} is the surface albedo and is set to be 0.25. $R_s \downarrow$ is the instantaneous downwelling shortwave radiation. Instantaneous downwelling shortwave radiation will be calculated for the RRG understorey site based on the DST method. ε_{surf} is the surface emissivity which is set to be 0.95. ε_{atm_adj} is the LAI adjusted atmosphere emissivity for the RRG understorey area ($\varepsilon_{atm\_adjusted} = (1 - LAI) * \varepsilon_{atm} + LAI * \varepsilon_{surf}$, where ε_{atm} is assumed to be 0.85), for the Lignum and Subshrub areas, overstorey LAI is considered to be zero. σ is Stefan-Boltzmann constant, which is equal to 5.67×10⁻⁸ W/(m²K⁴). T_a and T_s are the air and surface temperature.

2.9.2 Upscaling from instantaneous ET maps to daily ET maps

Here we trial two approaches for the RRG understorey site. The application of daily ET mapping will be undertaken for all surfaces using the best performing approach.

The first approach is anchored by the station-based measurements based on the following equation:

$$\frac{ET^d_{(i,j)}}{ET^I_{(i,j)}} = \frac{ET^d_{(o)}}{ET^I_{(o)}} \tag{19}$$

where $ET^d_{(i,j)}$ and $ET^I_{(i,j)}$ are the daily and instantaneous ET in location *i, j*. $ET^d_{(o)}$ and $ET^I_{(o)}$ are the daily and instantaneous ET in the RRG station. This method is referred to as the daily uniform temporal ET ratio method.

The assumption of this approach is that the ratio of daily ET to instantaneous ET does not vary spatially over the same vegetation cover condition. This way, the spatially continuous instantaneous ET map and the temporally continuous ET observation at the station can be incorporated to produce a daily ET map.

The second approach is anchored on the evaporative fraction, as shown in equation (20)

$$\frac{ET^d_{(i,j)}}{R^d_{n(i,j)}} = \frac{ET^I_{(i,j)}}{R^I_{n(i,j)}} \tag{20}$$

where $ET^d_{(i,j)}$ and $ET^I_{(i,j)}$ are the daily and instantaneous ET at location *i, j*. $R^d_{n(i,j)}$ and $R^I_{n(i,j)}$ are the daily and instantaneous net radiation map in the RRG understorey. This method is referred to as the daily constant evaporative fraction method in this report.

Here, we assume the evaporative fraction does not vary within a day for any location. This method requires spatially distributed daily net radiation data. We developed an empirical relationship for

27

estimating daily net radiation based on overstorey leaf area index and the weather condition, explained in section 2.9.3.

2.9.3 Daily net radiation mapping

A regression model is developed to map understorey daily net radiation. Based on our understanding of the factors influencing net radiation, we choose daily ambient weather conditions, including air temperature, relative humidity, downwelling shortwave radiation, and local LAI as predictor variables. We assume daily net radiation is linearly dependent on local LAI. The dependent variable of this regression function is the daily mean net radiation, as shown in the following equation:

$$R_n^d = b_0 + b_1 T_a + b_2 q_s + b_3 R_s + b_4 LAI_{10} \tag{21}$$

where R_n^d (W/m^2) is the mean daily net radiation, $b_0 - b_4$ are the coefficients, T_a (°C) and q_s (kg/kg) are ambient mean daily air temperature and specific humidity (measured at 3 m height), R_s (W/m^2) is downwelling shortwave radiation for the open surface. LAI_{10} is the focal mean LAI using a 10 m moving window. The regression equation and result are shown in Figure 11.

$$R_n^d = 1.18T_a + 2708.56q_s + 0.43R_s - 27.66LAI_{10} - 80.2$$
$$r^2 = 0.79$$
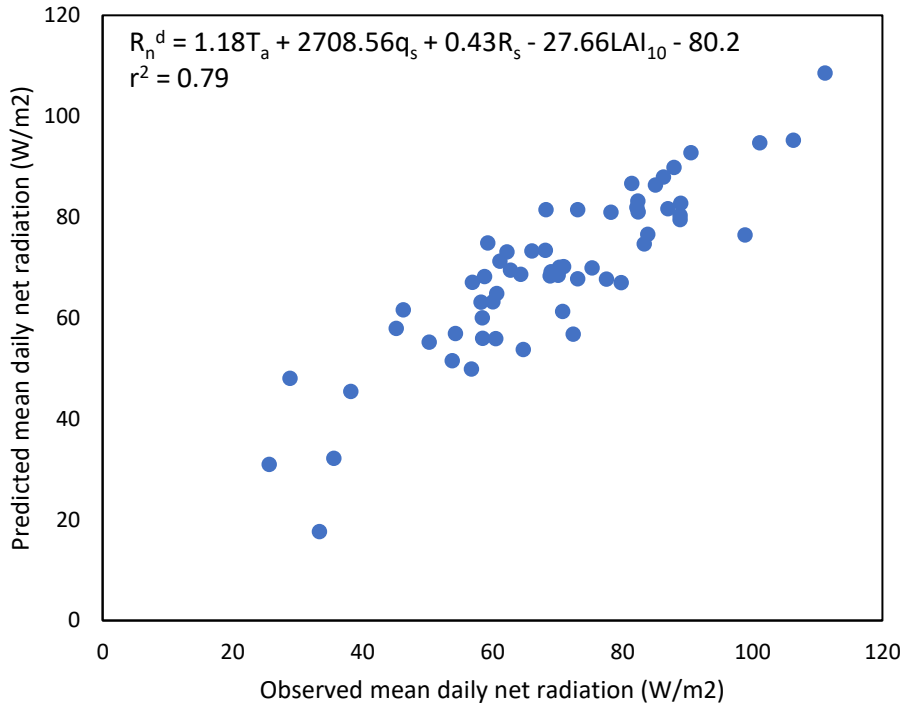
Figure 11 Scatter plot of observed mean daily net radiation and predicted mean daily net radiation based on multiple linear regression.

2.9.4 Mapping method evaluation

The instantaneous and daily understorey ET mapping results will be assessed by MEP ET estimation at selected iButton points in the RRG woodland. For each iButton point, half-hourly net radiation is calculated based on the method described in 2.9.1. The surface radiative temperature is missing for the iButton site, which is estimated by using:

$$\frac{T_a(i)}{T_s(i)} = \frac{T_a(o)}{T_s(o)} \tag{22}$$

where T_a and T_s are the air and surface temperature, *i* and *o* represent the iButton and station, respectively. Daily ET at each iButton point is calculated as the sum of half-hourly ET over 24-hour duration.

29

2.10 Monthly ET mapping

We use two methods to estimate monthly ET for diverse land cover types. For the surfaces without overstorey vegetation (Lignum and Subshrub sites), the observed ratio of monthly to daily from the corresponding station is used to upscale the daily ET map to monthly ET map (equation 23). For the understorey area, we adjust the daily to monthly ET ratio by considering the specific LAI at each location in relation to the LAI values at known station sites (equation 24).

$$\frac{ET^m_{(i,j)}}{ET^d_{(i,j)}} = \frac{ET^m_{(B/L)}}{ET^d_{(B/L)}} \tag{23}$$

$$\frac{ET^m_{(i,j)}}{ET^d_{(i,j)}} = \frac{LAI_{(i,j)}}{LAI_{(U)}}\frac{ET^m_{(U)}}{ET^d_{(U)}} + (1 - \frac{LAI_{(i,j)}}{LAI_{(U)}})\frac{ET^m_{(B)}}{ET^d_{(B)}} \tag{24}$$

where $ET^m_{(i,j)}$ and $ET^m_{(i,j)}$ are the monthly and daily ET of location (i,j), B, L, and U refer to the Subshrub, Lignum, and RRG understorey station measurement.

3 Results and Discussion

3.1 Summary of field data collection

3.1.1 MEP station data

Figure 12 illustrates the periods of data availability for three MEP stations. Each station has at least one-year of data from November 2021 to October 2022. Over this period, the area received 312 mm rainfall (data provided by CSIRO Doody's team). In anticipation of a flooding event in November 2022, all stations were retrieved from their field locations to prevent potential damage. The Subshrub and RRG stations were successfully reinstalled in April 2023. Unfortunately, the Lignum station was partly damaged, and some sensors were lost. After repair, it resumed monitoring in June 2023. A few iButton sensors were deployed at the respective locations as a substitute for the lost sensors to continue data collection. All stations have been actively recording data up to November 2023.
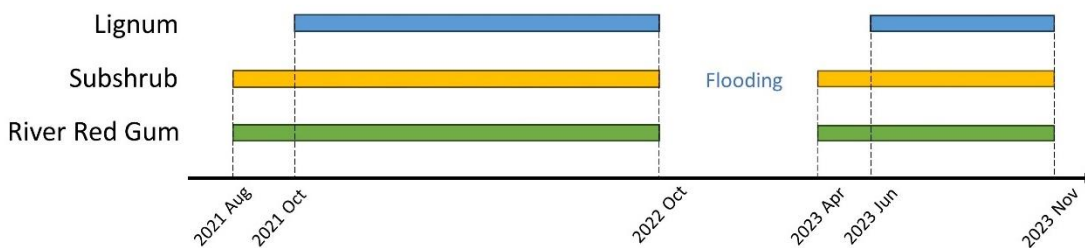
Figure 12 MEP station data records for three stations, the gap is due to the 2022-2023 River Murray flooding.

3.1.2 Drone-based thermal imaging

Table 1 lists all drone surveys conducted in our study area. The initial three surveys were primarily focused on testing equipment and refining flight plans, serving as practice runs. Throughout 2022, all thermal imaging was carried out twice daily, capturing surface temperatures in both the morning and afternoon. In 2023, the thermal surveys were limited to midday sessions. This adjustment was based on the finding that the estimation of surface specific humidity (section 2.7) is optimal when surface radiative temperature is captured around noon.

Table 1 A summary of drone missions undertaken for the project.

Time	Mission	Remote pilot
2021/11/23	Thermal survey (test)	Keane
2021/12/14	Thermal survey (test)	Keane
2022/02/03	Thermal survey (test)	Gutierrez-Jurado
2022/03/03	LiDAR survey	Keane
2022/03/04	Thermal survey	Gutierrez-Jurado and Keane
2022/04/10	Thermal survey	Gutierrez-Jurado
2022/05/07	Thermal survey	Gutierrez-Jurado
2022/06/25	Thermal survey	Gutierrez-Jurado
2023/04/11	LiDAR survey	Liu and Keane
2023/05/27	Thermal survey	Liu
2023/07/26	Thermal survey	Liu
2023/09/13	Thermal survey	Liu
2023/10/18	Thermal survey	Liu
2023/11/16&17	Thermal survey	Liu

3.1.3 Scattered temperature and humidity measurements

Table 2 shows the installed location and data collection period of the iButtons. These iButtons were set to record temperature and humidity data at 30-minute intervals. Each iButtons was placed in a radiation shield to avoid any direct radiation impact that could elevate temperature readings. Most of the iButton data were collected from August 2021 to November 2022. For the purposes of MEP modelling, iButtons 5-10 and 35-38 were chosen due to their proximity to the surface, ensuring the most relevant and accurate environmental measurements for the MEP-Evaporation method.

Table 2 IButton installation and data recording periods.

ID	Latitude	Longitude	Site	Measurement height (m)	Data period (Year/Month)
3	-34.360795	140.580109	Subshrub	0.6	2021/08 – 2022/11
4	-34.3591929	140.5779291	RRG	0.15	2021/08 – 2022/11
5	-34.35913687	140.5780883	RRG	0.15	2021/08 – 2022/11
6	-34.35911442	140.578402	RRG	0.15	2021/08 – 2022/11
7	-34.35898316	140.5786607	RRG	0.15	2021/08 – 2022/11
8	-34.35906462	140.5789615	RRG	0.15	2021/08 – 2022/11
9	-34.35858454	140.5787284	RRG	0.15	2021/08 – 2022/11
10	-34.35853947	140.5787555	RRG	0.15	2021/08 – 2022/11 (2022/06 and 2022/07 are missing)
11	-34.35844101	140.5787484	RRG	0.15	2021/08 – 2022/11
12	-34.35828312	140.5788067	RRG	0.15	2021/08 – 2022/11
13	-34.35827726	140.578605	RRG	0.15	2021/08 – 2022/11
14	-34.355209	140.58113	Lignum	0.15	2021/08 – 2022/05
15	-34.355067	140.580923	Lignum	0.15	2021/08 – 2022/09 (2022/06 is missing)
16	-34.355065	140.581436	Lignum	0.3	2021/08 – 2022/05
17	-34.360436	140.580225	Subshrub	0.15	2021/08 – 2021/09
18	-34.360926	140.57997	Subshrub	0.15	2021/08 – 2021/09
19	-34.360795	140.580109	Subshrub	1	2021/08 – 2022/11
20	-34.355192	140.581124	Lignum	1.5	2021/08 – 2022/09 (2022/06 is missing)
21	-34.355083	140.580919	Lignum	1.5	2021/08 – 2022/09 (2022/06 is missing)
22	-34.355096	140.581352	Lignum	1.5	2021/08 – 2022/09 (2022/06 is missing)

23	-34.355213	140.576839	Black Box	0.3	2021/09 – 2022/09
24	-34.355233	140.576801	Black Box	0.3	2021/09 – 2022/09
25	-34.35516	140.57672	Black Box	0.3	2021/09 – 2022/09
26	-34.35533	140.577093	Black Box	0.3	2021/09 – 2022/09
27	-34.355296	140.577197	Black Box	0.3	2021/09 – 2022/09
28	-34.355179	140.577305	Black Box	0.3	2021/09 – 2022/09
29	-34.355508	140.577293	Black Box	1.5	2021/09 – 2022/09 (2022/06 is missing)
30	-34.355557	140.577534	Black Box	1.5	2021/09 – 2022/09
31	-34.355597	140.577648	Black Box	1.5	2021/09 – 2022/11 (2022/06 and 2022/07 are missing)
32	-34.3555	140.57723	Black Box	0.3	2021/09 – 2022/09 (2022/06 is missing)
33	-34.355588	140.577551	Black Box	0.3	2021/09 – 2022/09
34	-34.355646	140.577625	Black Box	0.3	2021/09 – 2022/09
35	-34.360416	140.580201	Subshrub	0.15	2021/09 – 2022/11
36	-34.360435	140.580227	Subshrub	0.15	2021/09 – 2022/11
37	-34.360898	140.57995	Subshrub	0.15	2021/09 – 2022/11
38	-34.360926	140.579971	Subshrub	0.15	2021/09 – 2022/11

3.1.4 Other data

From October 2021 to February 2022, we used a Stevens Hydroprobe to monitor soil moisture at the Subshrub site. After that, from February to April 2022, we moved the Hydroprobe to the RRG site to measure its soil moisture. From May to August 2023, five TMS-4 soil moisture probes were installed at both Subshrub and RRG sites. Additionally, CO_2 concentration data was recorded at the Subshrub site during the whole study period. These data have not been analysed for this report. They are included in the project database for future use.

Soil samples were collected at the RRG, the Subshrub, and the Lignum sites on 17th August 2021 and 28th September 2021. The samples were analysed for soil salinity in the Ecohydrology Research Laboratory at Flinders University. Each soil sample was oven-dried to constant weight at 105 °C. A mixture of 20 g dry soil sample and 100 ml of deionised water was produced and shaken 100 times. After the sediment was settled, the specific electrical conductivity (EC) was measured in the supernatant using Eutech Oakton Cond 6+ Conductivity Meter. Altogether, 18 soil EC measurements were obtained, which are presented in Figure 1.

3.2 Comparison of the MEP-ET method and the Bowen Ratio Energy Balance method

The MEP-ET estimates are compared with those obtained using the BREB method. This comparison was conducted for both the Subshrub and the Lignum sites from November 2021 to October 2022.

3.2.1 Comparison at the Lignum site

The simulated half-hourly ET values are shown in Figure 13 for both MEP and BREB methods. For the BREB method, we use the temperature and humidity measurement at 3 m and 2.5 m heights. The range of MEP ET is larger than BREB ET. This difference is a reasonable reflection of the different footprint sizes of the two methods (meters for MEP, and tens to hundred meters for BREB). Another difference in the estimated half-hourly ET time series between the two methods is that the daily maximum half-hourly ET from the BREB method lacks seasonal variability, which does not seem to reflect the reality. Some spikes in BREB sub-hourly ET do not seem to be physically explainable either, which is considered a weakness of the BREB method. In this regard, the MEP method looks more robust. Its sub-hourly ET follows reasonable diurnal cycles and seasonal variability.

Figure 14 shows the BREB vs. the MEP half-hourly ET estimates with a blue 1:1 line. To insure the data quality, unreasonable Bowen ratio estimations are removed (*Perez et al.*, 1999). The plot reveals a close correlation between the MEP and BREB results, although MEP estimates are slightly lower than those from BREB. This difference is likely related to the different footprints of the two methods, and to the fact that the ground heat flux measurement for the BREB method was taken at a 5 cm depth, being lower than those at the ground surface.
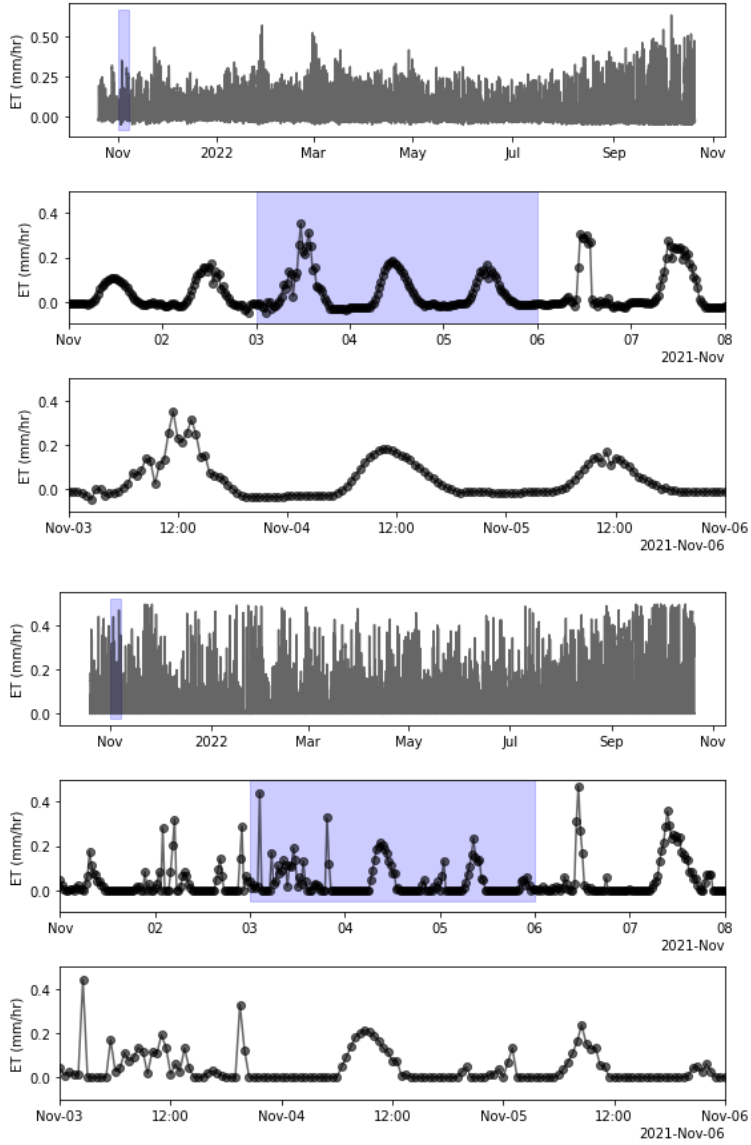
Figure 13 MEP (upper three panels) and BREB (lower three panels) simulated half-hourly ET for the Lignum site. The blue sections show the insets for the relevant zoom-in graphs.
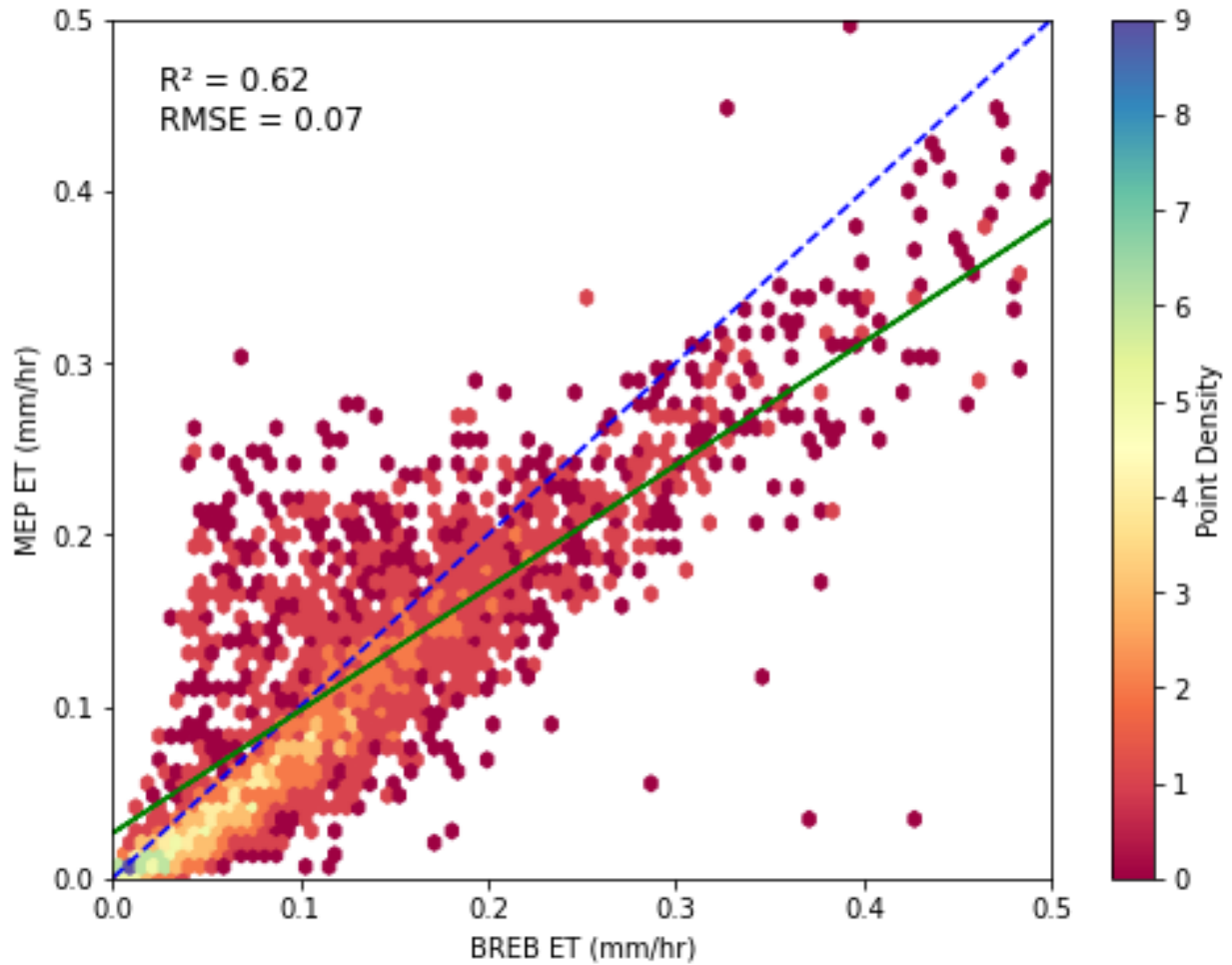
Figure 14 Scatter density plot of MEP and BREB hourly ET estimates for the Lignum site. The blue line is the 1:1 line and the green line is the linear fitting line.

3.2.2 Comparison at the Subshrub site

At the Subshrub site, temperature and humidity were measured at two elevations (0.3 and 1 m), and net radiation was recorded for the site. Unfortunately, ground heat flux was not available. To enable the comparison, the MEP estimated ground heat flux was used as an input for the BREB method. In this case, the comparison of the two methods can be viewed on how the two methods partition the available energy (R_n - G).

Figure 15 shows both MEP and BREB estimated half-hourly ET at the Subshrub site. The MEP-derived ET time series exhibits significant seasonal variation, with higher ET rates during the summer and lower rates in the winter. This pattern is consistent with expected seasonal dynamics and likely reflects actual

37

conditions. Conversely, the BREB estimation of daily maximum half-hourly ET demonstrate limited seasonal variation. This discrepancy can be attributed to the inherent instability of the Bowen ratio, which may result in anomalously high ET values. Such extremes can obscure the seasonal fluctuation in the BREB-derived ET estimates, making the seasonal variability less apparent.
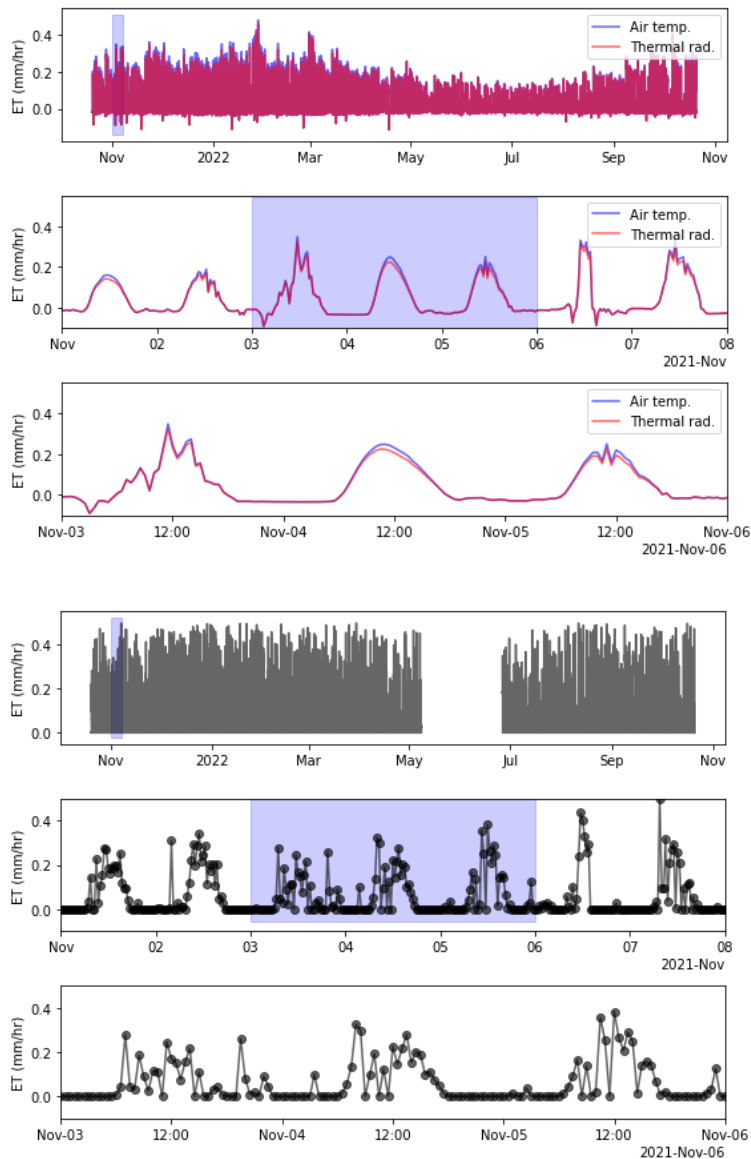
Figure 15 MEP (upper three panels) and BREB (lower three panels) simulated half-hourly ET for the Subshrub site. Two surface temperature measurements (thermal infrared and air temperature were applied for the MEP method. The blue sections show the insets for the relevant zoom-in graphs.

Figure 16 shows the MEP-ET half-hourly estimates in comparison to the BREB estimates for the Subshrub site. It is observed that the BREB method generally yields higher ET estimates than the MEP method. This discrepancy could be attributed to the positioning of the temperature and humidity sensors used in the BREB method, which are possibly too close to the Subshrub canopy, which may result in an overestimation of latent heat, thus leading to higher ET readings. Another possibility is associated with the instability problem of the BREB method under some conditions. As discussed by (*Payero et al.*, 2003), the Bowen ratio method can become unstable when the Bowen ratio is close to -1, which frequently occurs close to sunrise and sunset. To avoid this problem, Bowen ratio values <-0.75 and >-1.25 were rejected (following *Tanner et al.* (1987)). However, *Payero et al.* (2003) note that although this approach is effective at removing most erroneous estimates, some outliers may remain. Erroneous estimates with the BREB method may be potentially leading to some overly high ET estimates that are not matched by the MEP approach.
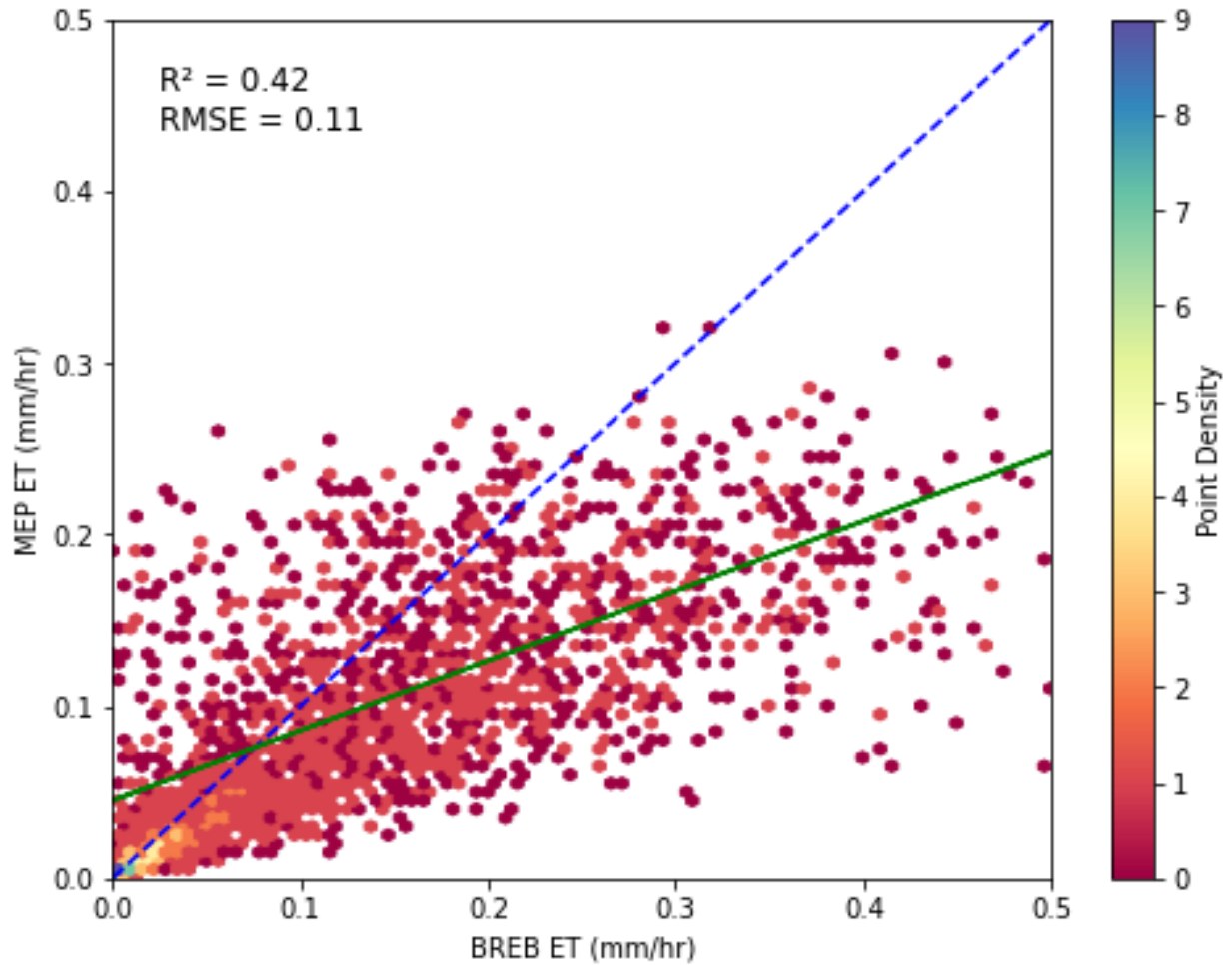
Figure 16 A scatter density plot of MEP and BREB hourly ET estimates for the Subshrub site. The blue line is the 1:1 line and the green line is the linear fitting line.

3.3 ET estimation at the three stations

Data required for the MEP ET modelling have been collected at the RRG understorey and Subshrub site since August 2021, and at the Lignum site since October 2021. To maintain consistency in our analysis, we simulated ET for all three station locations from October 2021 to November 2023. It is important to note that during and in a couple of months after the flooding, the ET estimations are absent due to missing data.

3.3.1 ET estimation for the Lignum station

At this site, both MEP-Evaporation and MEP-Transpiration models were applied. For the transpiration model, we adopted use of a stress index (SI) similar to crop water stress index (Liu et al. 2021) for

representing Lignum shrub water stress in calculating the σ function. The SI is calculated based on measured canopy temperature and air temperature (*Liu et al.*, 2020). It has a value between zero and one. A value of one means a complete stress condition under which the vegetation ceases to transpire. A value of zero means the vegetation transpires at the potential transpiration rate. Figure 17 shows a time series of daily SI for the Lignum site. It shows that a decent size of rainfall can relieve Lignum shrubs' water stress greatly. However, this temporal stress relief does not last more than a week. It also shows that SI decreases on some days without observed rainfall. One possibility is that on those days, the atmospheric demand for evaporation is low (e.g., resulting from cloud cover and high humidity), which can relieve plant water stress (*Liu et al.*, 2017; *Yang et al.*, 2013).
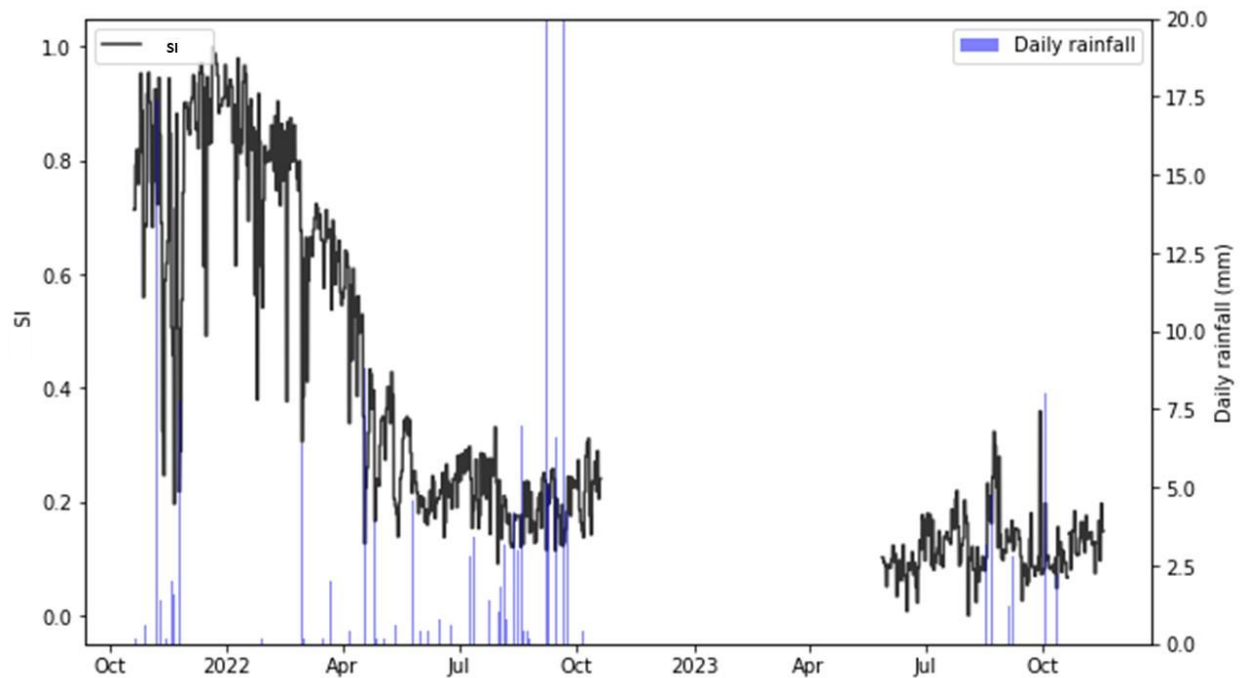
Figure 17 Calculated daily SI for the Lignum canopy, together with observed daily rainfall at the site.

Simulated daily ET from 20-10-2021 to 16-11-2023 is shown in Figure 18. Daily ET varies from 0.5 mm/day to 3 mm/day. The mean daily ET is estimated to be 1 mm/day from 20-10-2021 to 20-10-2022. Figure 19 shows the monthly ET estimation from November 2021 to October 2023. Winter ET is lower than in other seasons.
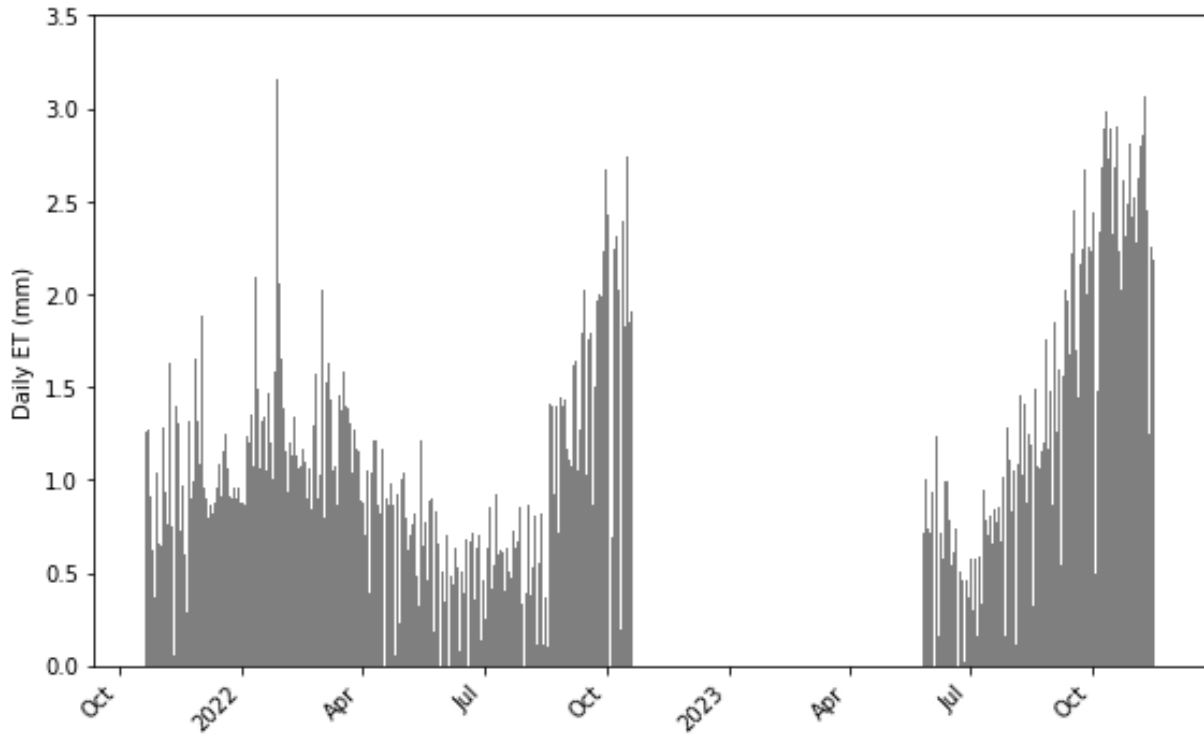
Figure 18 MEP estimated daily ET from late October 2021 to November 2023 for the Lignum site.
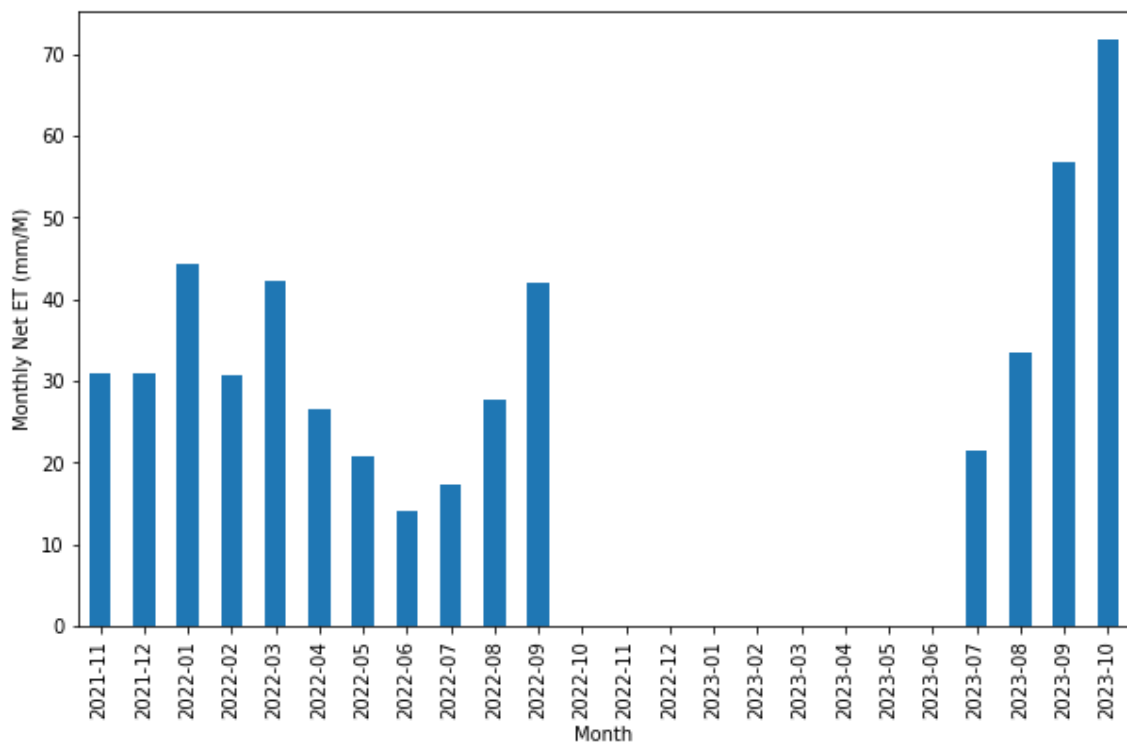
Figure 19 Monthly ET at the Lignum station (the months of missing data are not shown).

Simulated daily ET for the Subshrub station from the MEP method is shown in Figure 20. Over the whole period, daily ET varies from below 0.5 mm/day to around 2.5 mm/day. The mean daily ET is estimated to be 0.79 mm/day from 20-10-2021 to 20-10-2022. Based on the MEP estimates, evapotranspiration at this site is 0.3 mm/day lower than the Lignum site from 20-10-2021 to 20-10-2022. Figure 21 shows the monthly ET simulation result from November 2021 to October 2023. Clear seasonal variability is shown. The highest monthly ET is about eight times that in the lowest month.
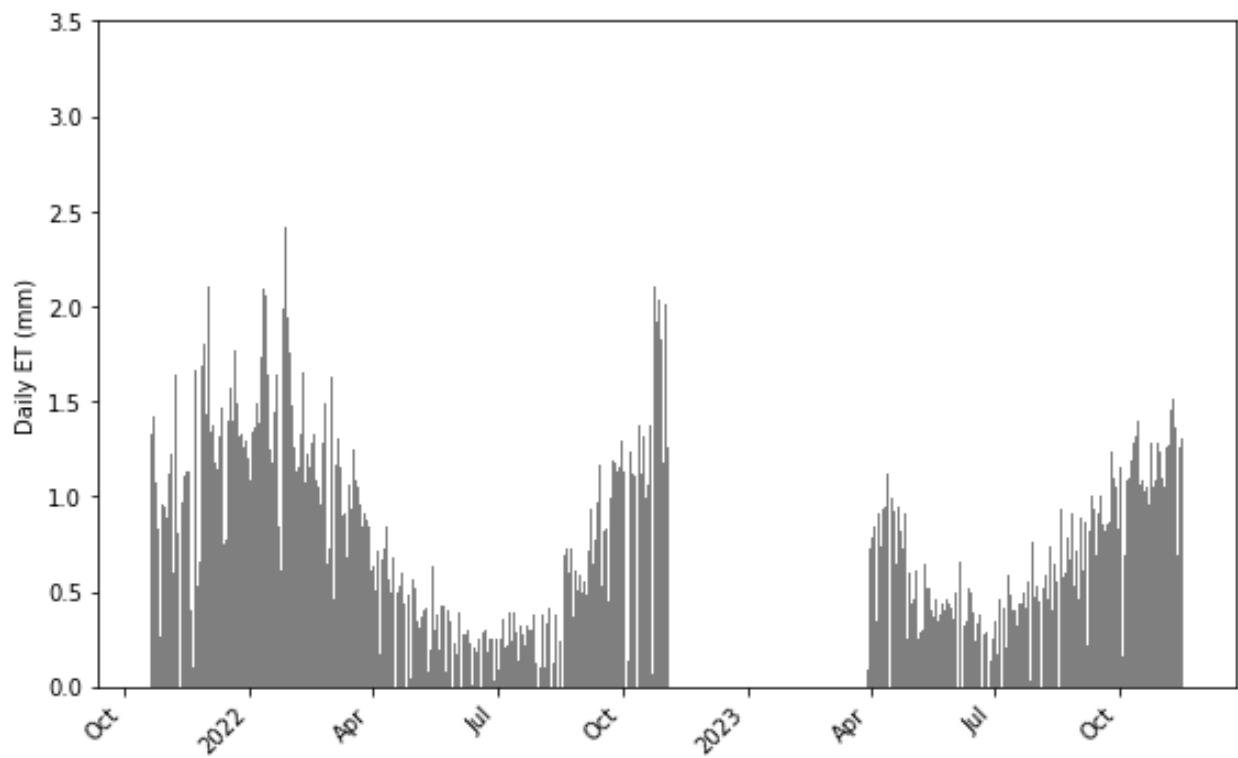
Figure 20 MEP estimated daily ET from late October 2021 to November 2023 for the Subshrub site.
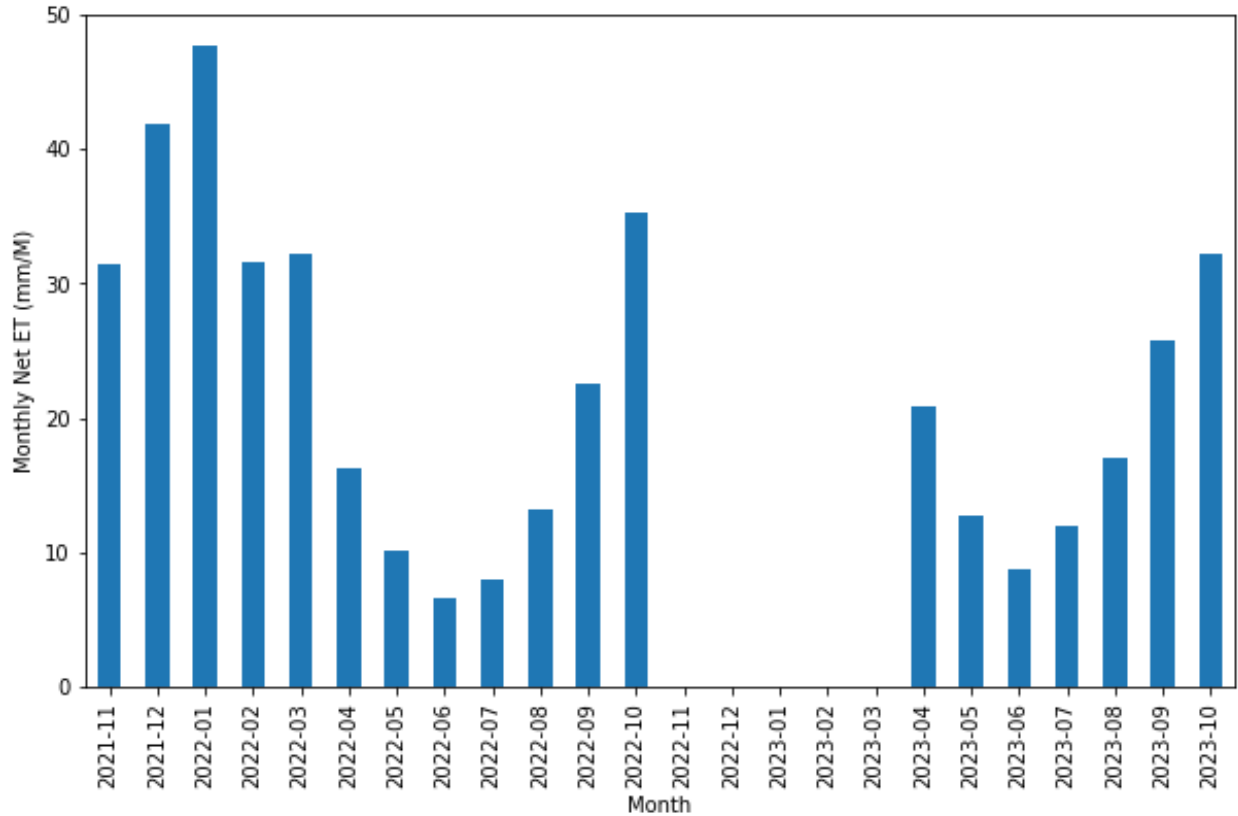
Figure 21 Monthly ET of the Subshrub station (the months of missing data are not shown).

3.3.3 ET estimation for the RRG understorey

Figure 22 shows the daily ET at the RRG understorey station, as estimated using the MEP method. During the observation period, the daily ET ranges from less than 0.25 mm/day to slightly over 1.5 mm/day. The average daily ET is 0.52 mm/day for the year-long period from 20-10-2021 to 20-10-2022. According to these MEP estimates, the RRG site experienced an evapotranspiration rate that was about 0.5 mm/day lower than that of the Lignum site for the same period. Additionally, Figure 23 shows the monthly ET from November 2021 to October 2023. A clear seasonality in ET occurs at this site, with the largest monthly ET rate being over ten times the value of the lowest month. Among all the stations, the RRG understorey site recorded the lowest ET, which can be attributed to the reduced energy input to the understorey surface.

44
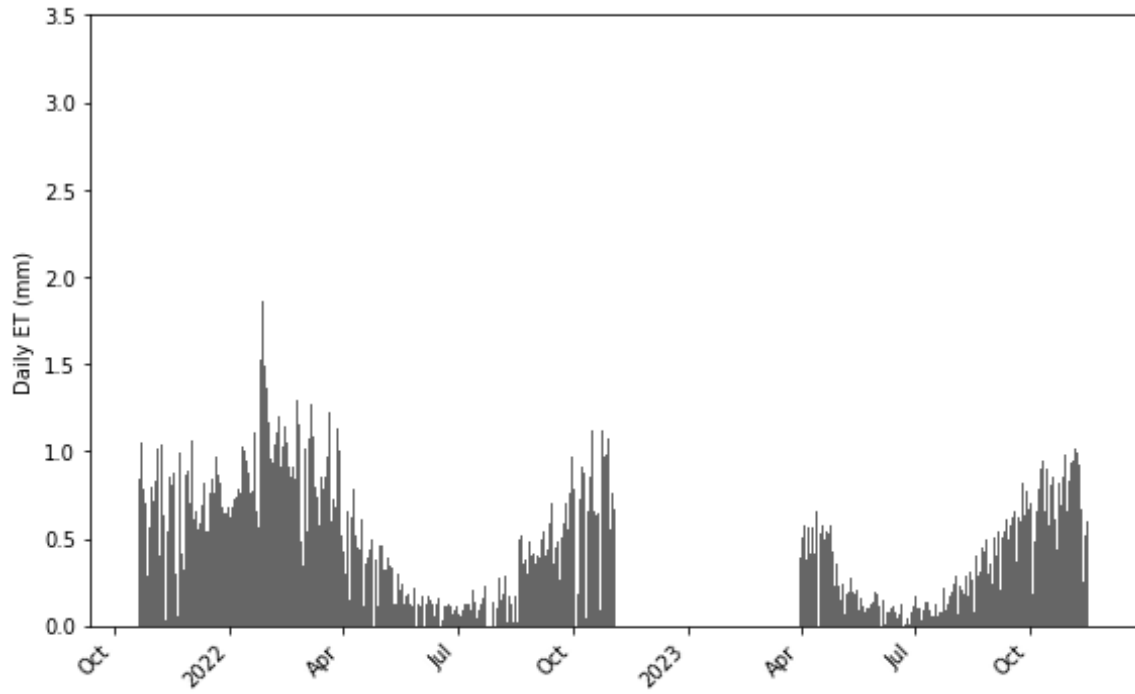
Figure 22 MEP estimated daily ET from late October 2021 to November 2023 for the RRG understorey site.
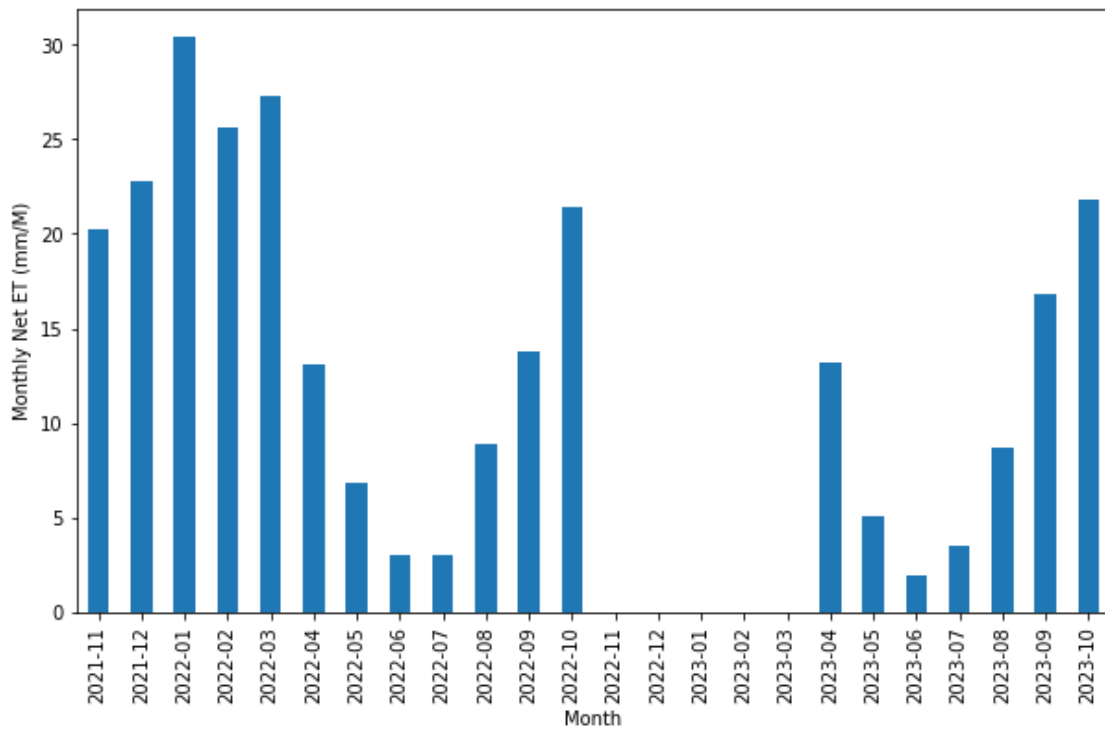
Figure 23 Monthly ET of the RRG understorey station (the months of missing data are not shown).

Figure 24 shows the distribution of daily ET for each season at the three MEP stations. Generally, the ET rate is highest in summer and lowest in winter for each site. For the Lignum site, the seasonal variation is relatively small. The median values are relatively close from spring to autumn.

The Subshrub and RRG understorey sites exhibit a comparable seasonal pattern, characterised by higher daily ET rates during the summer months and lower ET rates in autumn and winter, reflecting the effects of typical seasonal fluctuations in temperature and solar radiation.
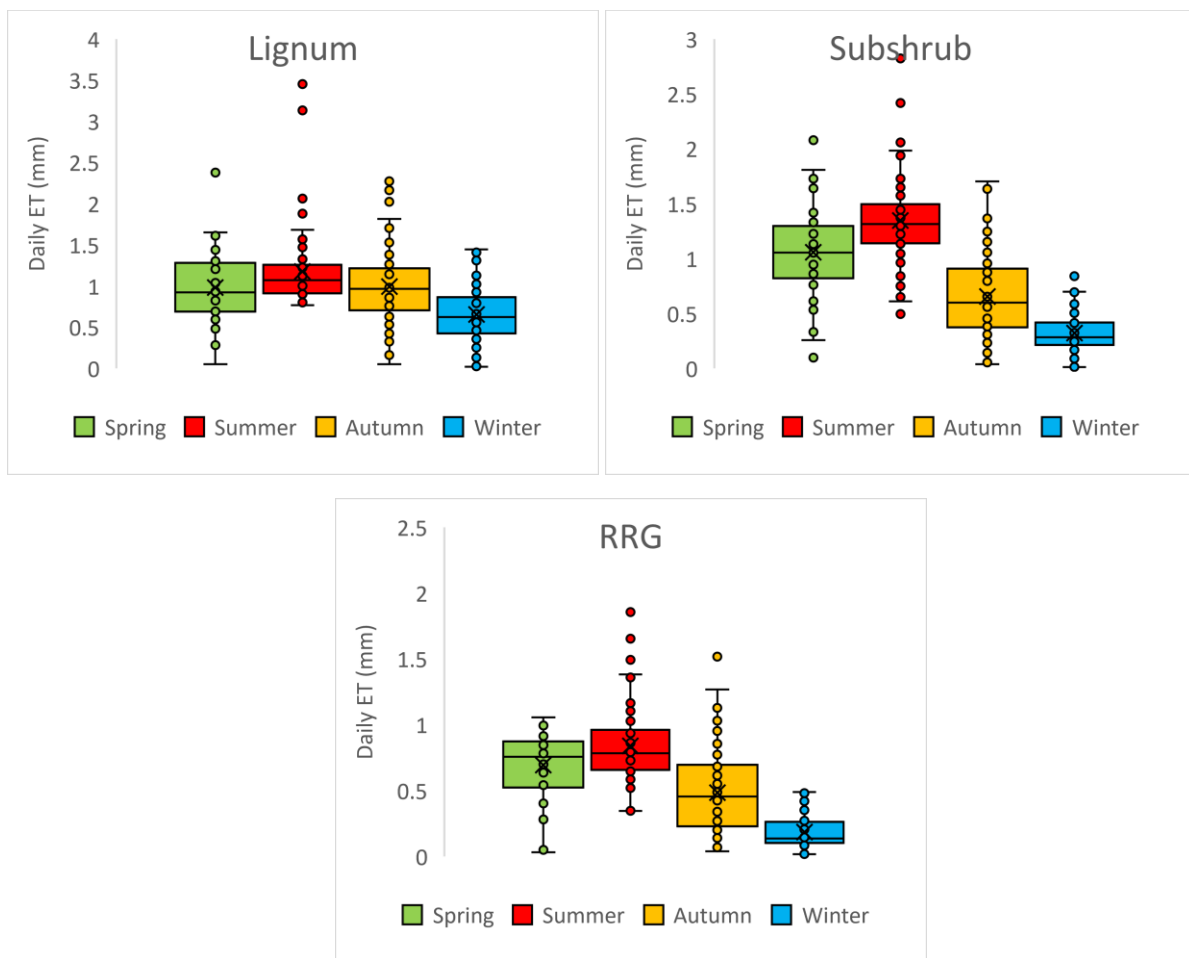
Figure 24 Daily ET distribution for different seasons at the three stations (Spring: Oct/2021-Nov/2021, Summer: Dec/2021-Feb/2022, Autumn: Mar/2022-May/2022, Winter: Jun/2022-Aug/2022).

3.3.5 Flooding impact on ET

During the project, a large River Murray flood occurred from late 2022 to early 2023. Figure 25 shows the upstream water level recorded at Lock 4 of the River Murray, approximately 2 km upstream from the study area (https://riverdata.mdba.gov.au/lock-4-upstream). The red dots show the elevations of MEP stations in the study area. The Lignum site, which is situated at the lowest elevation among these stations, was impacted by the flooding in early October 2022. The Subshrub site was influenced by the rising waters in November, followed by the RRG site in December 2022. Although the water level at Lock 4 returned to its baseline by March 2023, residual water persisted in some of the study sites until April 2023.
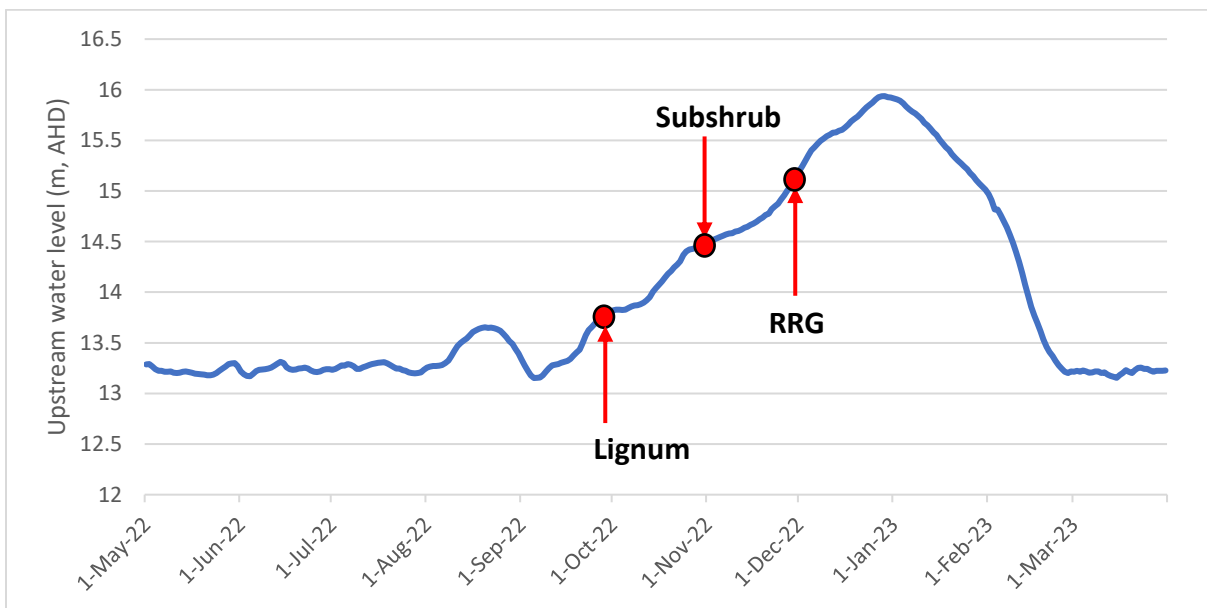
Figure 25 Upstream water level (AHD) and the elevation of the three stations.

Figure 26 shows the amount and percentage changes of monthly ET before and after the flooding event (months with incomplete data are not shown). At the Lignum site, a significant increase in ET occurred after the flooding. The peak difference occurred between Septembers of the two years. About 40% more September ET was observed in 2023 (several months after the flood event) than in 2022. This surge in ET was likely associated with the regrowth of Lignum vegetation following the flood.

The flooding initially resulted in substantial mortality among the Lignum plants, which should have temporarily reduced transpiration rates due to the decreased plant leaf area. However, the abundant water availability post-flooding, coupled with the emergent growth of grasses, likely compensated the reduction of Lignum shrub transpiration, thereby sustaining higher overall ET levels. In the early spring (September) of 2023, the surge Lignum regrowth further boosting ET at this site.
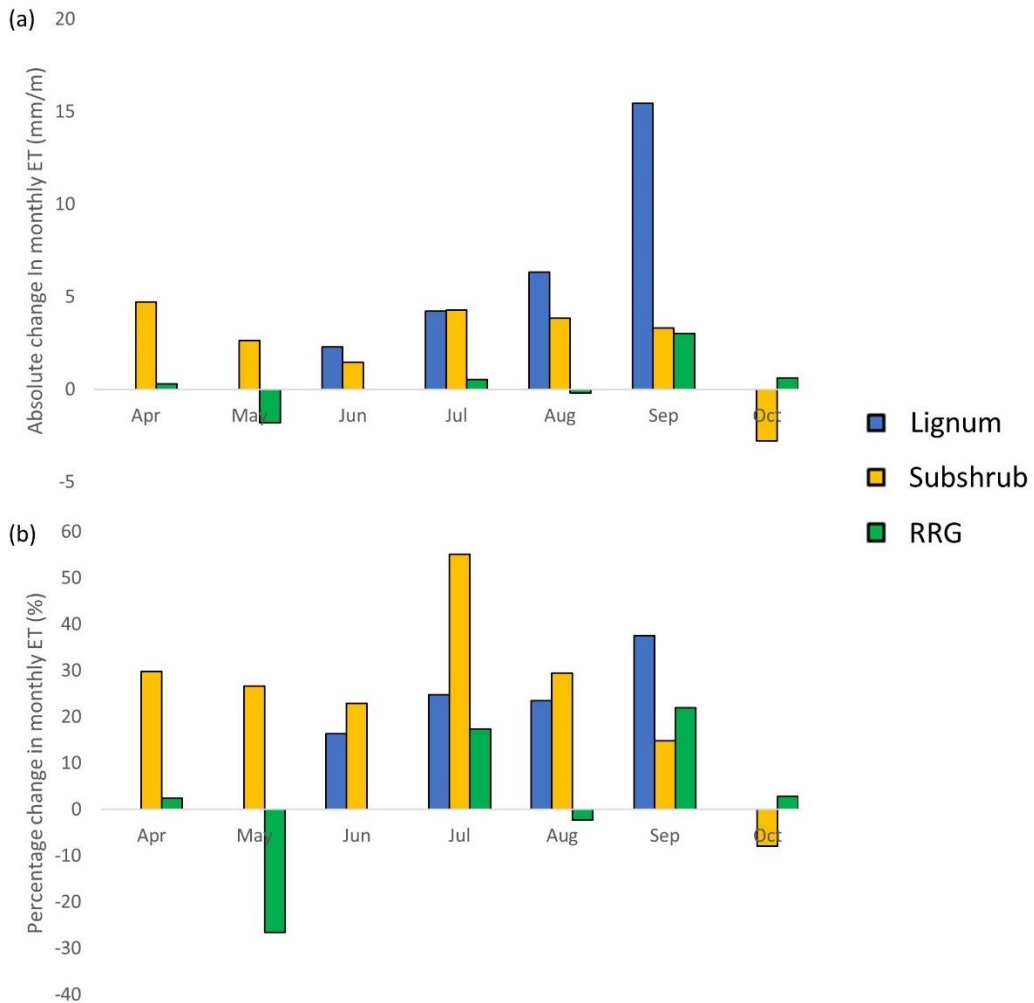
Figure 26 (a) Absolute and (b) Percentage change in monthly ET before and after the 2022-2023 Murray River flooding.

At the Subshrub site, a distinctive pattern in ET change was observed following the flooding event. From April to September, ET increased from the corresponding months of the previous year, with a peak change in July 2023 when ET increased 50% from July 2022. According to the monthly rainfall data from BOM (http://www.bom.gov.au), the rainfall in June 2022 and June 2023 was 11.9 and 34.8 mm, respectively. The elevated moisture in the soil, due to both residual water from the flooding and the increased rainfall in 2023, was likely responsible for the MEP estimated ET changes between the two years. However, from August to October 2023, a significant reduction in rainfall was observed – only 50%, 5%, and 10% of the previous year's levels. This decrease in rainfall led to reduced soil moisture, resulting in a corresponding decrease in ET rates. This pattern suggests that the impact of the flooding on the Subshrub site was relatively short and that the ET dynamics at this site are more directly influenced by the precipitation input.

At the RRG understorey site, monthly ET did not change from that in the corresponding month before the flood. This is very likely related to the sandy soil and limited energy input due to the overstorey canopy. The sandy soil allows for a quick percolation of excess water from the flooding. The canopy provides a stable microclimate by moderating temperature, humidity, intercepting solar radiation and rainfall.

3.4 MEP-ET estimation at the iButton locations

ET was estimated at 10 iButton locations (Figure 27) at the Subshrub site and the RRG understorey site using the observed (for Subshrub) or modelled (RRG understorey) radiation and the temperature and humidity measured at each iButton location. For the Subshrub site, the iButton sensors were installed either next to short vegetation or away from vegetation. For example, iButton 36 and 38 were located next the Subshrub vegetation, while 35 and 37 were located over bare ground. For the RRG understorey site, the ground vegetation cover and shading condition are different among the iButton locations.

Table 3 provides the monthly total ET for each iButton location. For the RRG understorey, iButton 8 shows the highest ET, with an average ET of 39.2 mm/month and a standard deviation of 14.9 mm/month. In contrast, iButton 6 has the lowest ET and variability, with a mean ET of 24.2 mm/month and a standard deviation of 10.6 mm/month. Generally, the ET estimates appear to increase from November to January, then decrease afterwards. This is likely to do with the available radiation (i.e., more daylight in the summer) and the occurrence of rainfall events.

For the Subshrub site, iButton 37 records the highest ET, with a mean value of 32.4 mm/month, while iButton 17, 36 shows the lowest ET, recording a mean value of 30.8 mm/month. The seasonal pattern is the same with the RRG site. Interestingly, the measured monthly ET values are similar between the locations regardless their relative distance to the Subshrub plants. This suggests that the local temperature and humidity are not significantly influenced by the surrounding Subshrub plants.
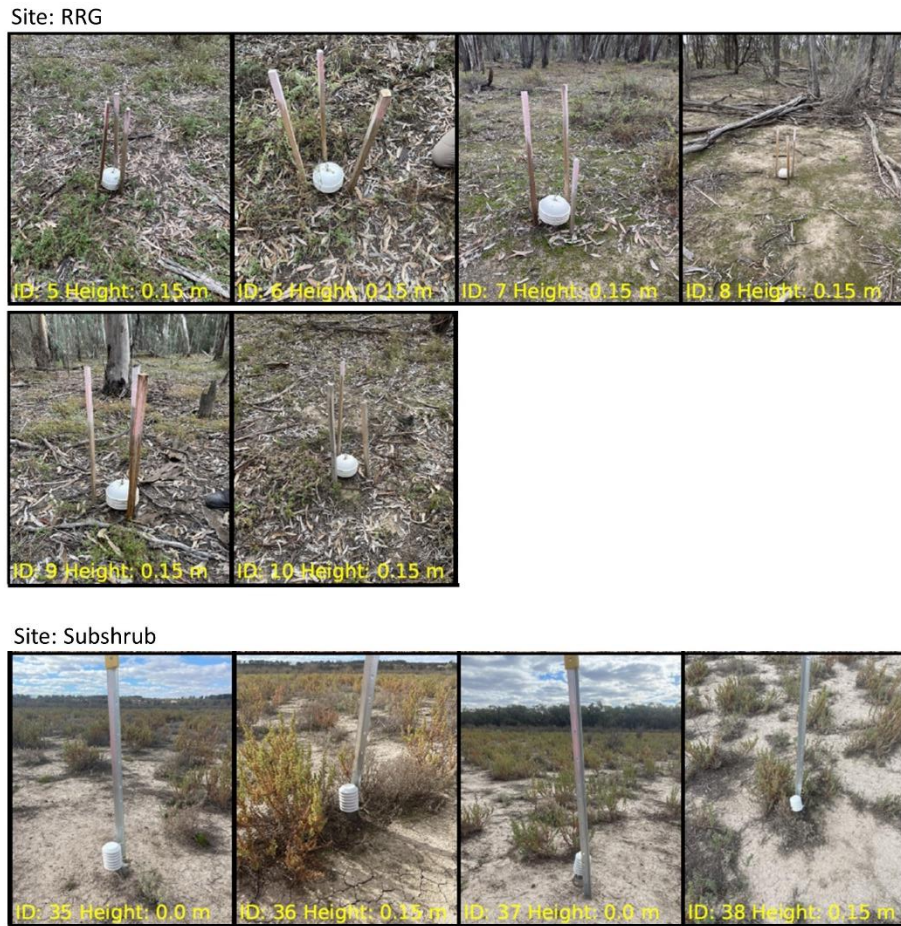
Figure 27 Photographs of the iButton sensors at the RRG understorey and Subshrub sites.

Table 3 Monthly average daily ET for each iButton site. Sensors 17 and 18 failed during the monitoring period and were replaced by sensors 36 and 38.

iButton ID	Site	Monthly Total ET (mm/month)											
		Nov 21	Dec 21	Jan 22	Feb 22	Mar 22	Apr 22	May 22	Jun 22	Jul 22	Aug 22	Sep 22	Oct 22
5	RRG	31.70	36.95	46.98	39.61	38.05	15.83	-	-	6.90	-	22.86	17.28
6	RRG	27.07	28.78	37.68	34.21	35.06	14.04	-	-	4.77	-	20.71	15.15
7	RRG	40.46	46.68	57.20	46.99	50.13	21.35	-	-	8.63	-	31.58	21.61
8	RRG	41.69	48.33	59.78	50.80	54.43	27.95	-	-	12.14	-	34.71	23.34
9	RRG	32.86	35.98	44.74	38.56	42.08	23.61	-	-	13.40	-	26.67	17.67
10	RRG	40.61	45.80	55.65	47.68	51.47	29.61	-	-	-	-	32.63	21.94
35	Subshrub	34.06	43.94	49.15	34.49	34.89	17.39	-	-	9.13	-	25.31	42.18
17, 36	Subshrub	34.02	43.66	48.62	33.96	34.53	17.22	-	-	9.16	-	25.27	-
37	Subshrub	34.18	44.00	49.05	34.49	34.84	17.33	-	-	9.15	-	25.46	42.96
18, 38	Subshrub	34.54	44.63	49.49	-	-	17.47	-	-	9.09	-	25.73	43.49

3.5 LAI, net radiation, temperature, and specific humidity mapping

In this section, spatial distributed input variables for MEP ET mapping are generated, including net radiation, surface radiative temperature, and surface specific humidity. Because the net radiation and surface temperature distributions are both dependent on overstorey canopy cover, an overstorey LAI map needs to be generated too.

3.5.1 LAI mapping

The LAI map is generated using the LiDAR point cloud data calibrated by field LAI measurement. We collected LAI data on 11 May 2022. Due to the unstable sky condition on the day, most measurements in the afternoon were found to be not useful. This report adopted the first set of measurements at the iButton points in the RRG understorey site.

Given that LAI field measurement and LiDAR estimation have different spatial resolutions. The field measured LAI is compared to LiDAR-derived LAI at 1 m, 3 m, and 5 m spatial resolutions. We found the LiDAR estimation at 1-m resolution having the highest correlation with the measured LAI as shown in Figure 28.

The figure shows a scatter plot with "Observed LAI" on the y-axis (ranging from 0 to 1.2) and "LiDAR estimation" on the x-axis (ranging from 0 to 2), with a dotted trend line and the equation:

$$y = 0.48x + 0.14$$
$$R^2 = 0.82$$
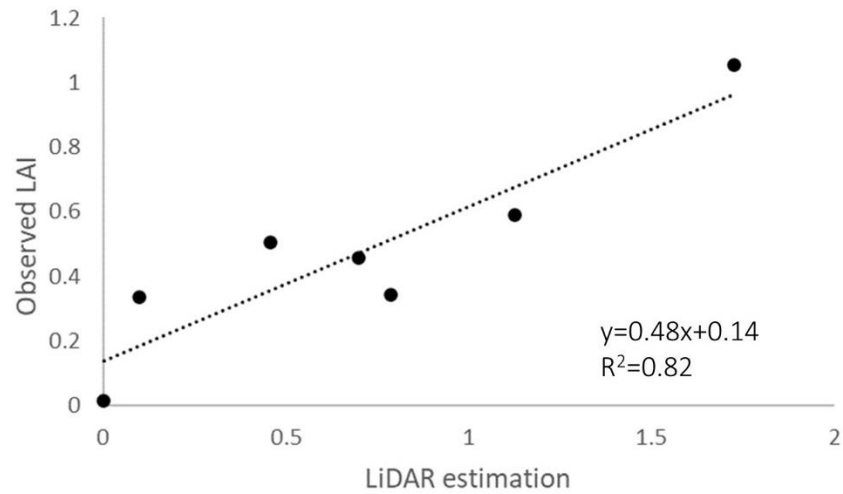
Figure 28 Scatter plot of LiDAR estimated LAI (1 m resolution) versus LP-80 measured LAI.

Based on the relationship derived in Figure 28, an LAI map of the RRG area is produced based on the LiDAR survey on 04/03/2022 (Figure 29). The map reveals spatially distributed overstorey vegetation cover, with higher LAI values in densely vegetated zones and lower values in open or sparsely vegetated zones. This variation is key to understanding the canopy's influence on microclimatic conditions, especially in terms of its shading effect on radiation.
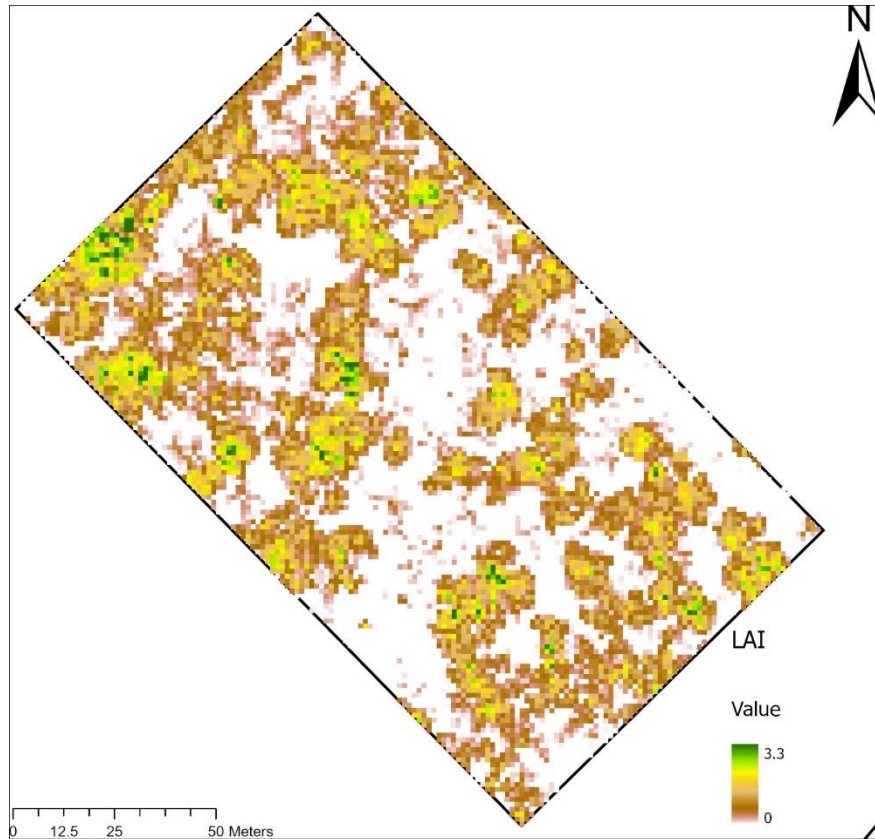
Figure 29 The LAI map of a section of the RRG woodland.

3.5.2 Understorey net radiation, surface temperature and specific humidity mapping

Mapped net radiation, surface temperature, and specific humidity are shown in Figures 30 and 31 for a cloudy day and a sunny day, respectively, to elucidate the impact of differing weather conditions on these key environmental variables for the MEP ET modelling. On the cloudy day (Figure 30), the net radiation values are noticeably low due to the reduced solar irradiance, leading to a generally cool surface across the study area. This cool surface is accompanied by relatively high specific humidity. In contrast, the sunny day (Figure 31) shows high net radiation. This increase in radiation results in elevated surface temperatures and low specific humidity.

The radiation spatial pattern in Figure 31 is different from that of Figure 30 due to the direct radiation casting in a certain angle on the sunny day. Given that this directional pattern varies with solar position in the sky, the pattern in Figure 31 for the drone survey time does not represent those in other hours of the day. This can pose challenges for upscaling instantaneous ET maps to daily and monthly ET maps. This issue will be further examined in detail later in this report.
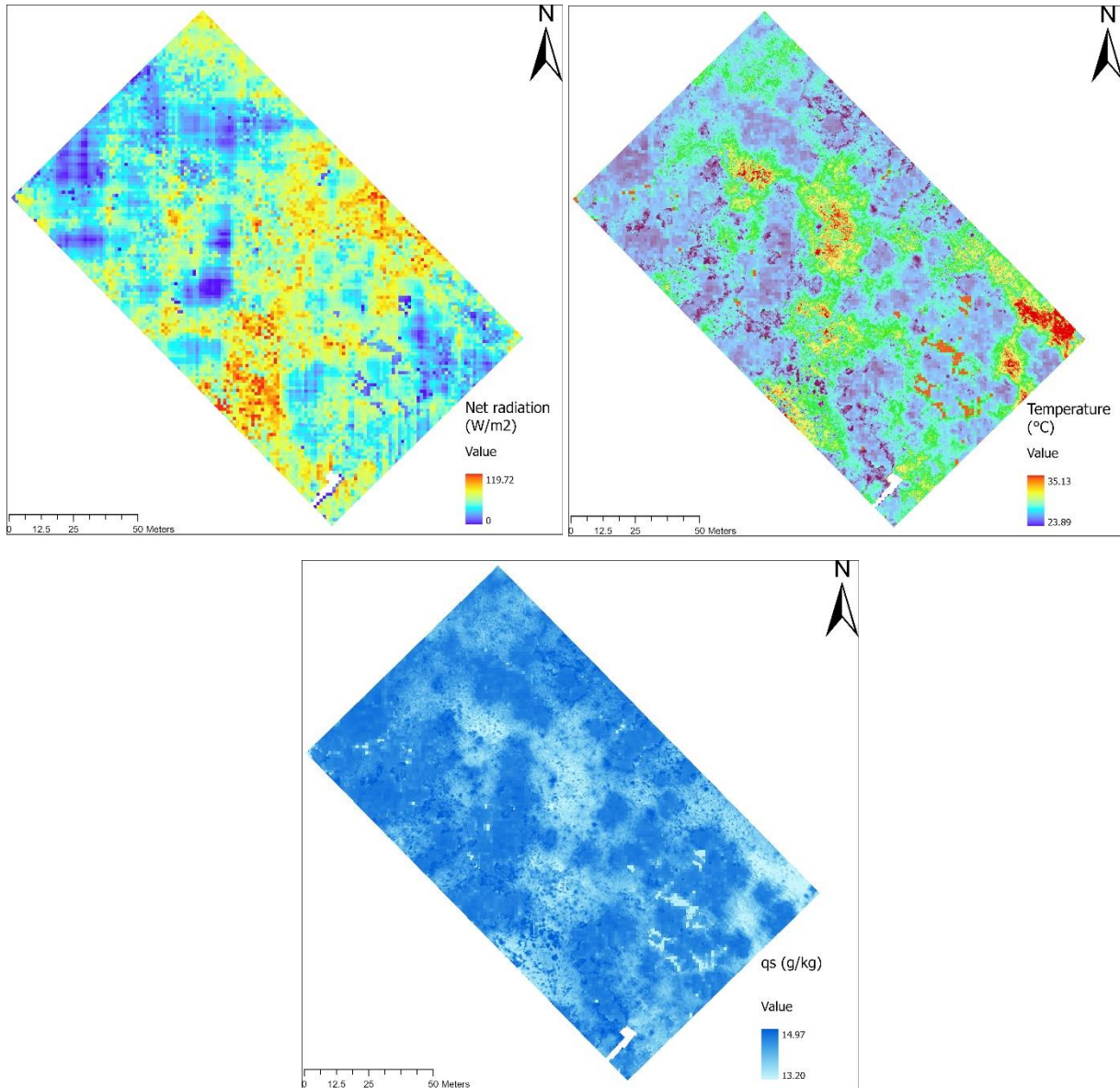
Figure 30 Modelled spatially distributed net radiation, surface temperature, and specific humidity at the RRG understorey for 15:00 on 04/03/2022.
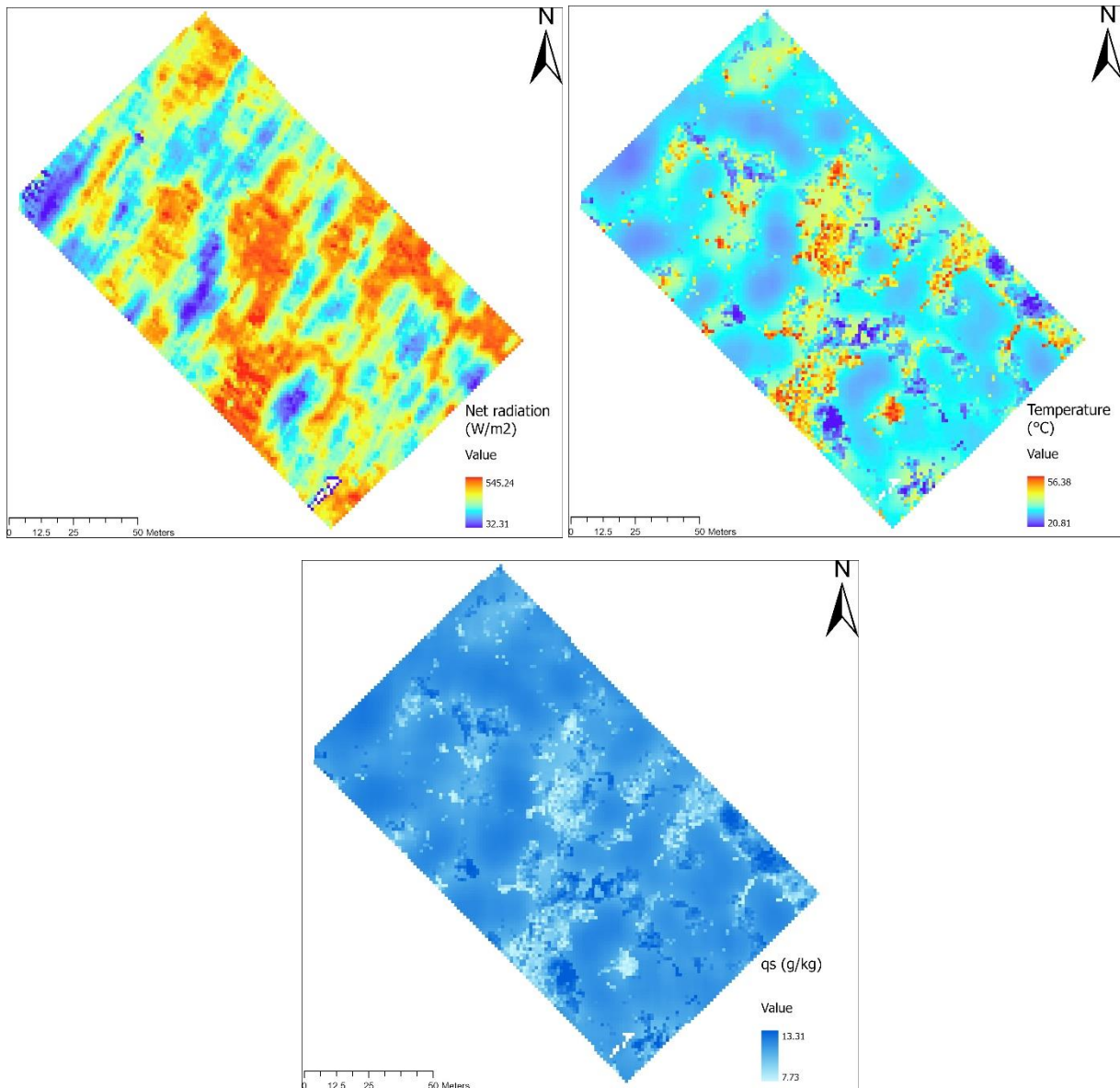
Figure 31 Modelled spatially distributed net radiation, surface temperature, and specific humidity at the RRG understorey for 10:30 on 10/04/2022.

3.5.3 Temperature correction for unstable sky condition

Drone thermal imaging is supposed to be undertaken under a stable sky condition. However, due to limitation of drone availability and short range of reliable weather forecasting, some drone thermal images were taken under unstable sky conditions. This can complicate the use of thermal imagery for MEP spatial modelling. Thermal cameras capture the energy emitted from the ground and object upon it, but a change of cloud cover can rapidly alter the ground temperature. When clouds intermittently

block direct sunlight, there's a notable drop in the energy reaching the ground, causing significant changes in the recorded temperature by a thermal camera. This variation results in abrupt changes in measured radiative temperature over the imaged area.

To address this issue, a histogram matching technique was employed. This method adjusts the temperature impacted by episodic cloud shading to the value as if it was under the sky condition of other sections of the area which were not impacted. The method categorises the imaging area into cloud-shaded sections and clear-sky sections. The clear-sky sections, which are not affected by cloud cover, serve as a reference for correcting the temperatures in the shaded areas. By applying this technique, it is possible to align the temperature distribution of the shaded sections to that of the reference sections, thus mitigating the effects of the unstable sky conditions on the thermal imagery. Figures 32 and 33 illustrate the temperature data before and after applying this method.
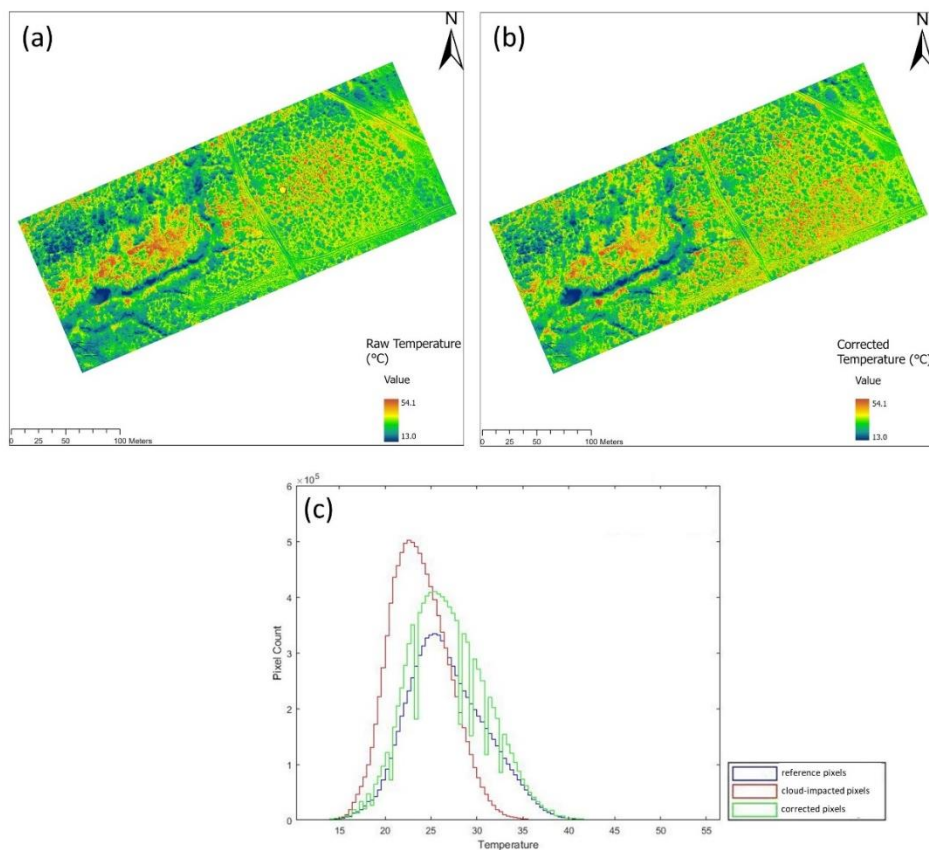
Figure 32 (a) Thermal image captured at 12:00 07/05/2022 for the Lignum site, (b) the corrected thermal image, and (c) the histograms before and after the correction.
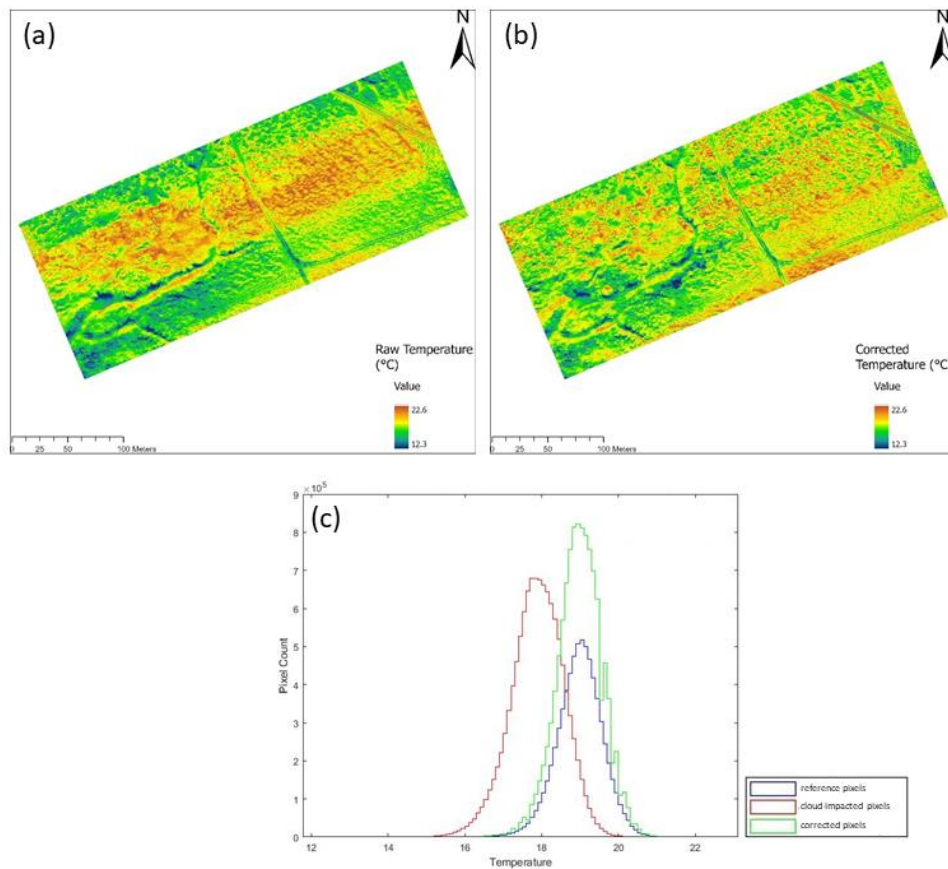
Figure 33 (a) The thermal image captured at 17:00 07/05/2022 for the Lignum area under an unstable sky condition, (b) the corrected thermal image, and (c) the histograms before and after the correction.

3.6 ET mapping

3.6.1 Instantaneous ET mapping

In this section, the instantaneous ET mapping using the MEP model is demonstrated. Figure 34 shows the modelled instantaneous ET at the RRG understorey for both a cloudy and a sunny day. It can be found that the sunny day's ET is higher than the cloudy day. The spatial distribution within the figure highlights that the ET is lower in the understorey regions compared to open areas, primarily due to reduced energy inputs in this shaded environment.

In Figure 34 (c) and (d), we compare the mapped ET values to the iButton instantaneous ET estimation. This comparison reveals a notable correlation between the two estimations. The correlation between these measurements is significant as it demonstrates the model's effectiveness in accurately capturing

ET variations in the RRG understorey. This result confirms the reliability of the mapping approach for the RRG understorey under different weather conditions.
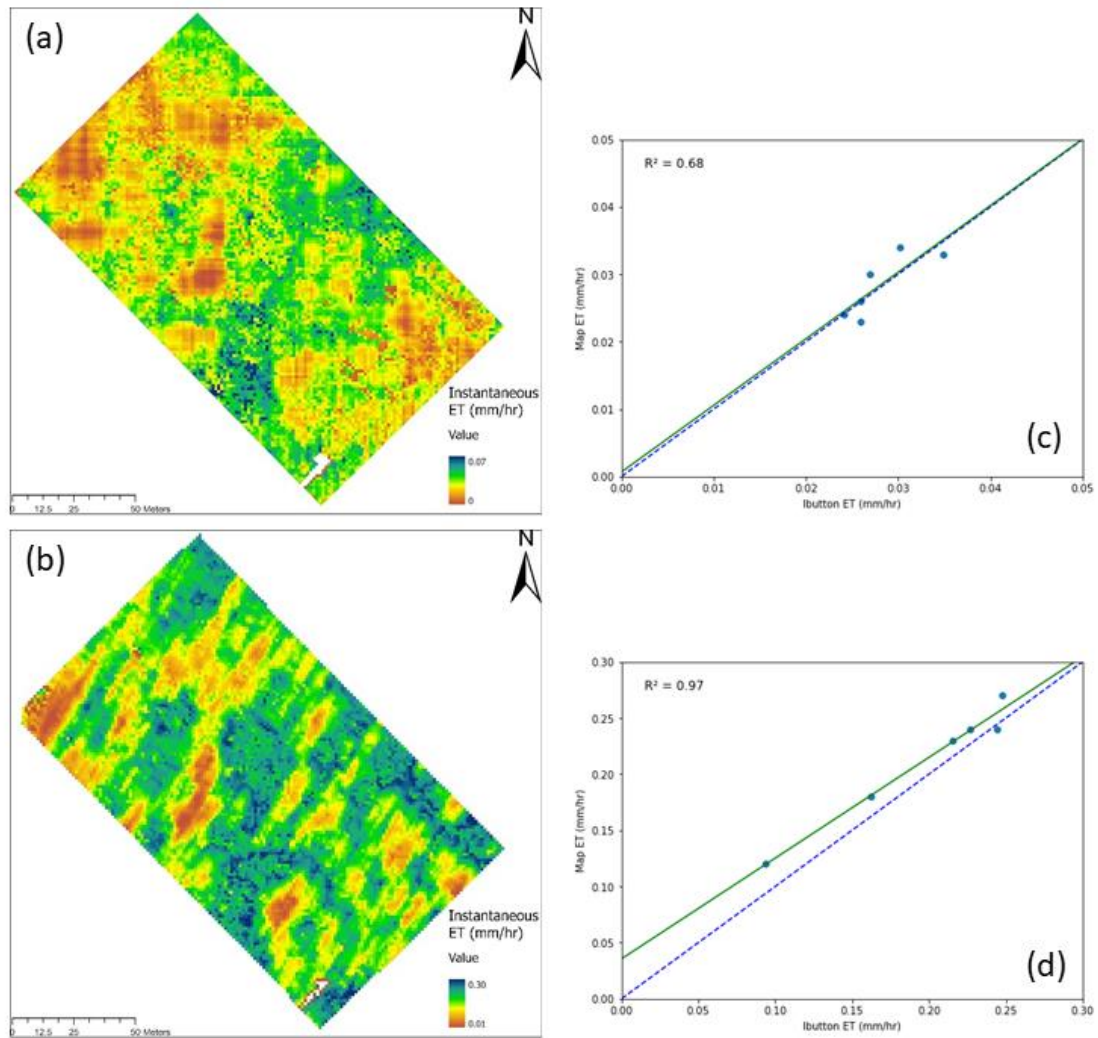
Figure 34 Instantaneous ET maps for (a) 15:00 04/03/2022 (cloudy day) and (b) 10:30 10/04/2022 (sunny day) of the RRG understorey area, and the scatter plots (c) and (d) of mapped ET compared with iButton estimated ET for the two image capturing times. The colour legends in (a) and (b) have different ranges.

Selected instantaneous ET maps for the Subshrub and Lignum areas are shown in Figure 35. In both areas where vegetation overstory is lacking, net radiation at the two areas was calculated according to Equation (18). The spatial variation of instantaneously ET in either area is a lot smaller than the RRG understorey area. Nevertheless, some spots in the Subshrub area show larger ET, which are likely the

spots where Lignum shrubs are present. For the ET maps of the Lignum areas, the flooding channel appears to have a larger ET than the surroundings. For both areas, the roads are observable on the ET maps due to more uniform ET distribution. This demonstrates the effectiveness of our drone imagery in reliably capturing ET variations for the short vegetation areas.
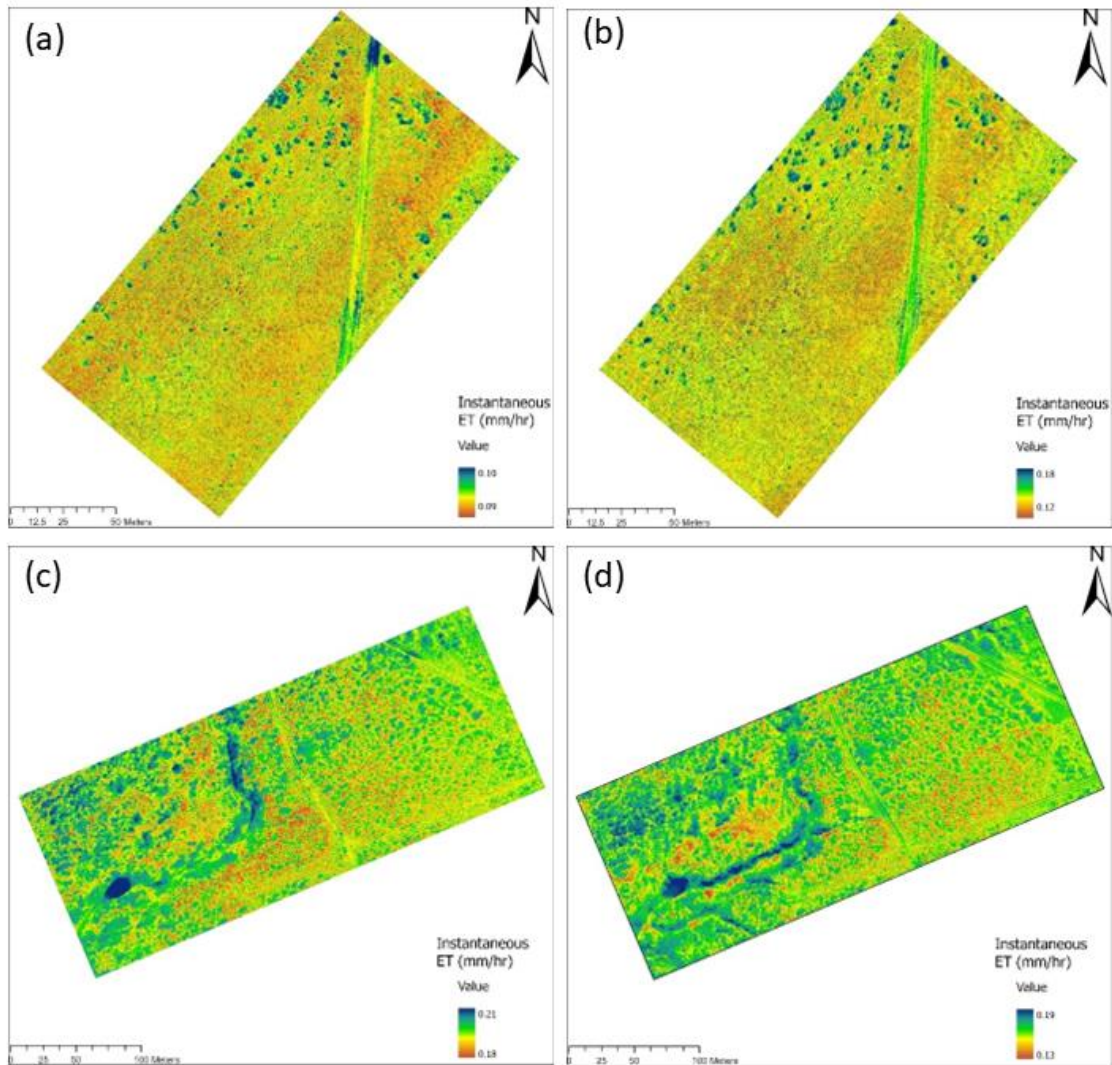
Figure 35 Instantaneous ET maps for the Subshrub area (a) 14:30 on 04/03/2022, (b) 11:30 on 10/04/2022 and the Lignum area (c) 10:30 on 04/03/2022, and (d) 11:30 on 07/05/2022. The colour legends have different ranges.

3.6.2 Daily ET mapping

Figures 36 and 37 display the upscaled daily ET maps for the RRG understorey, using the uniform ET ratio method, and the constant evaporative fraction method, respectively. The scatter plots comparing the

daily ET estimates from iButton data with the mapped ET values. It is observed that the daily ET maps upscaled using the uniform ET ratio method having spatial patterns consistent with the corresponding instantaneous ET, whereas the maps based on the constant evaporative fraction do not. This result suggests that the uniform ET ratio method is more suitable than the constant evaporative fraction method for the studied RRG understorey.
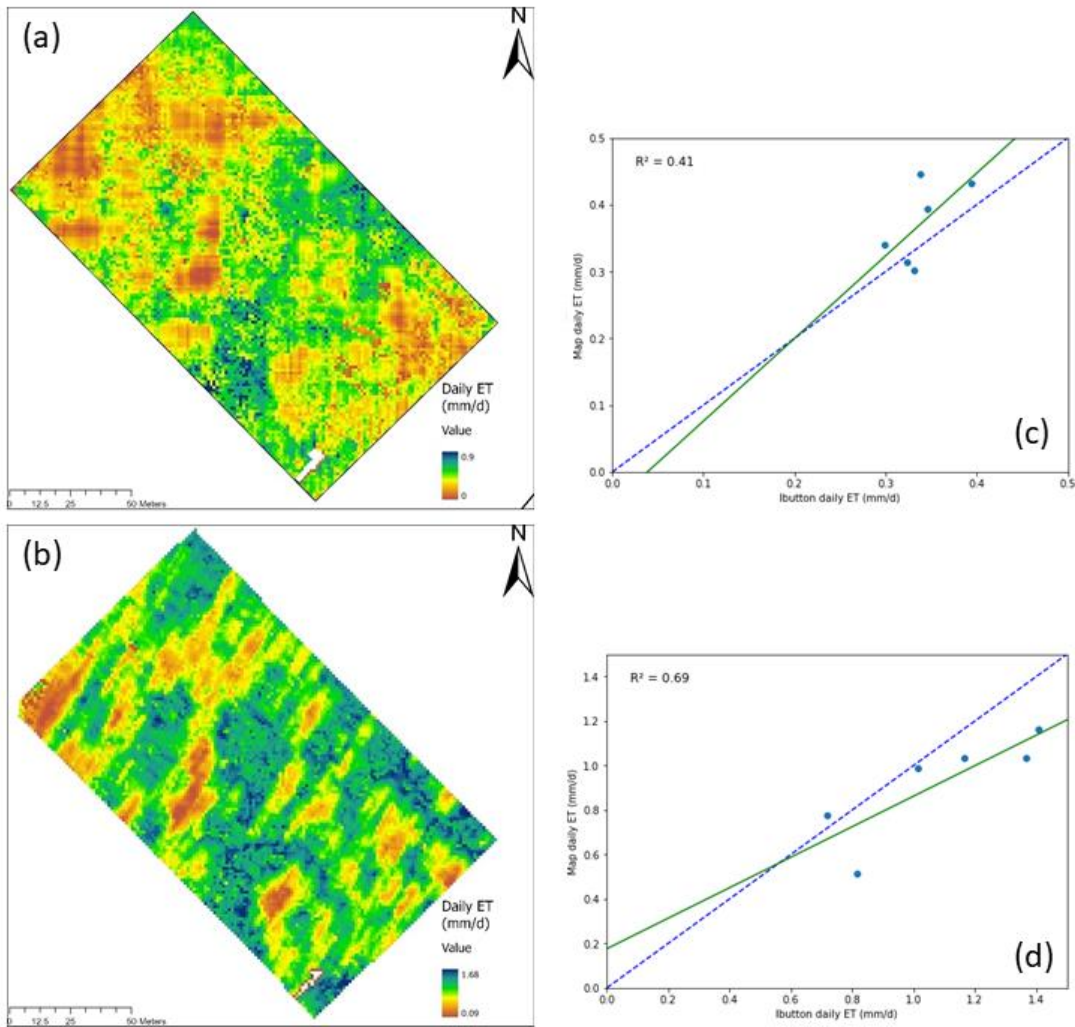
Figure 36 Daily ET maps for (a) 04/03/2022 (cloudy day) and (b) 10/04/2022 (sunny day) at RRG understorey based on the uniform ET ratio method, and the scatter plots (c) and (d) of mapped ET compared with daily ET estimated from the iButton measurement of the two days. The colour legends have different ranges in (a) and (b).

Figure 36 reveals an issue with the upscaled daily ET on sunny days. The instantaneous ET, calculated using net radiation at a specific moment, reflects the directional influence of sunlight at that time. While this approach is suitable for creating instantaneous ET maps, it is not suitable for daily ET mapping. Therefore, we recommend conducting drone thermal surveys around noon so that the directional canopy shadow effect is minimised. If this cannot be done, two thermal surveys should be undertaken, one in the morning and the other in the afternoon. The daily ET map can then be generated using the average of the two, as demonstrated in Figure 38.
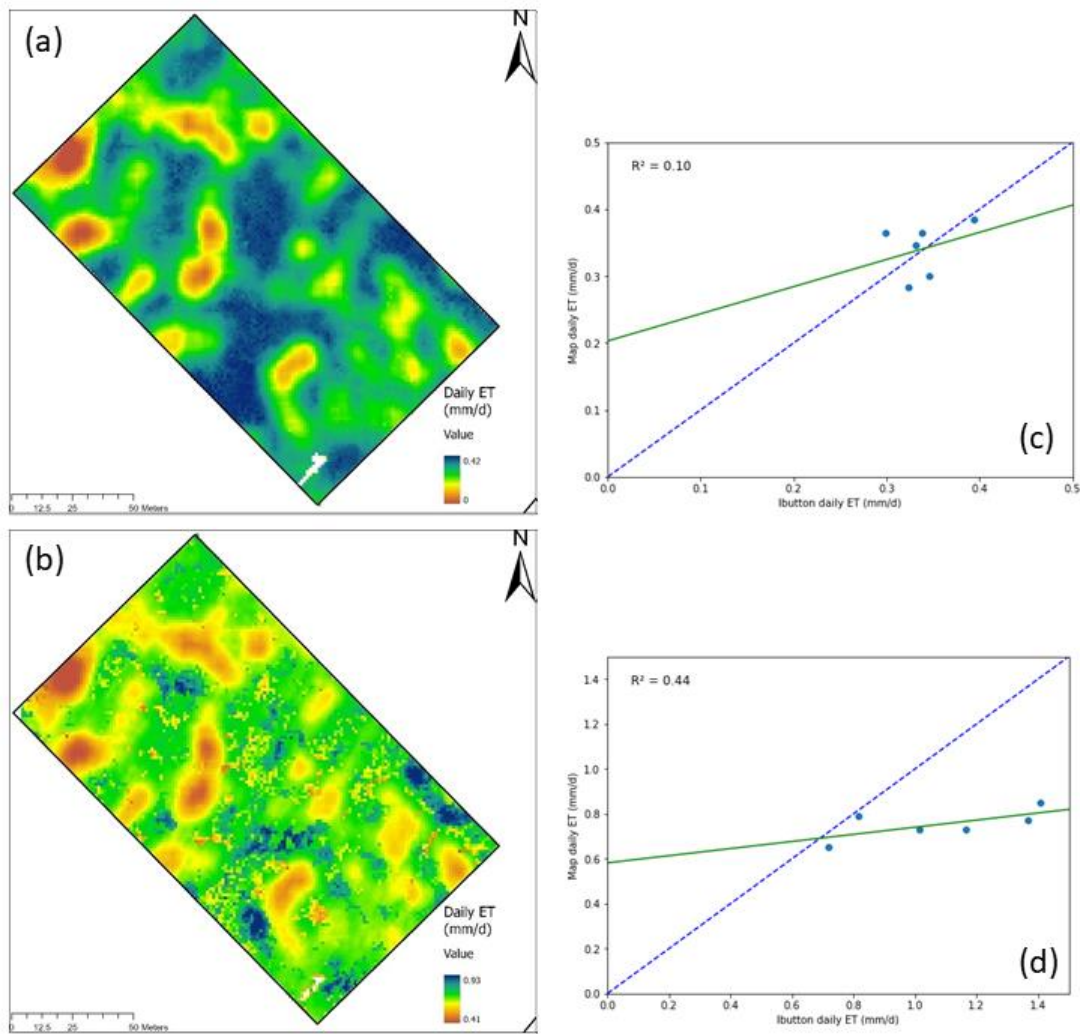
Figure 37 Daily ET maps for (a) 04/03/2022 (cloudy day) and (b) 10/04/2022 (sunny day) at the RRG understorey based on the constant evaporative fraction method, and (c) and (d) the scatter plots of mapped ET compared with daily ET estimated from the iButton measurement. The colour legends in (a) and (b) have different ranges.
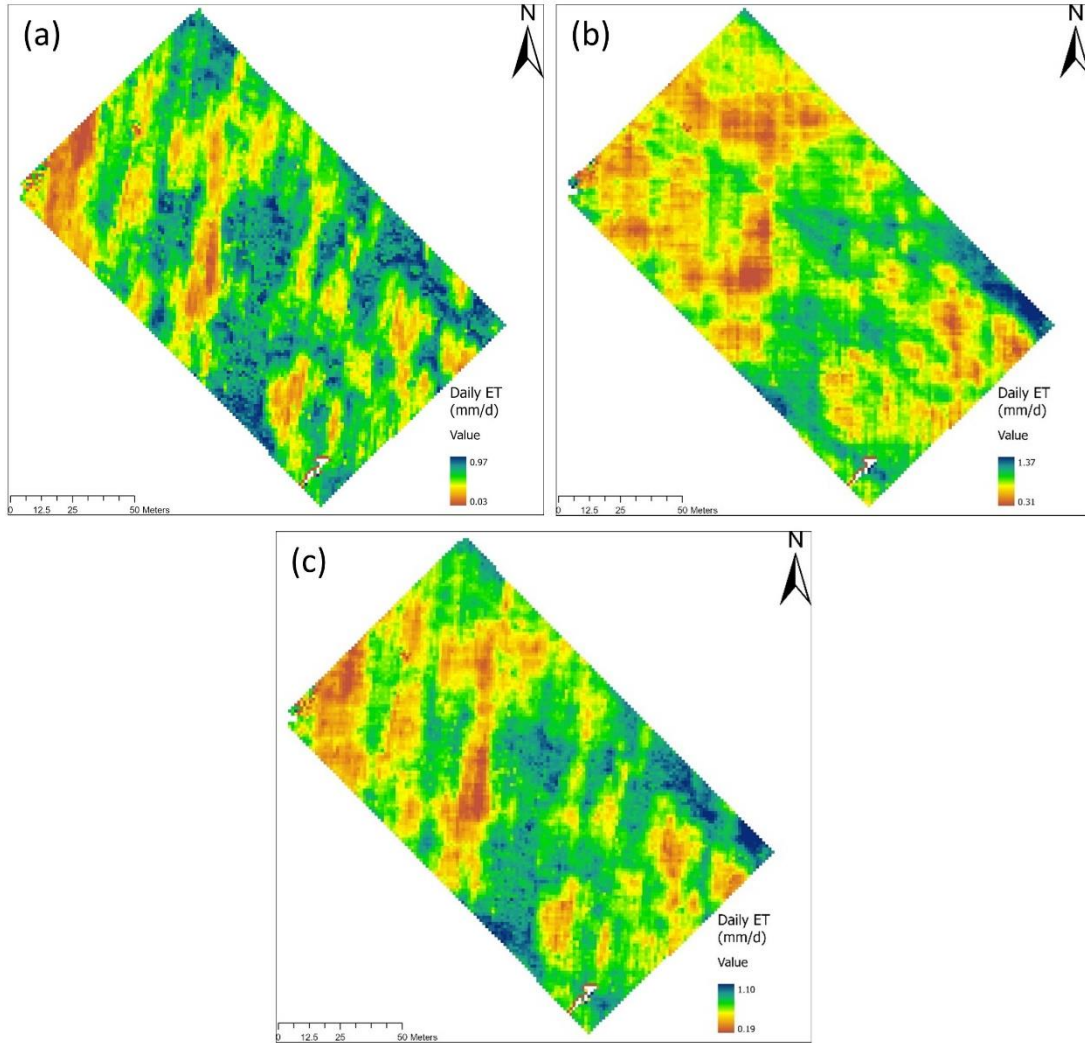
Figure 38 Daily ET maps (a) based on the morning (11:30) imagery and (b) based on the afternoon (15:30) imagery at RRG understorey on 07/05/2022, and (c) the average of the two. The colour legends have different ranges.
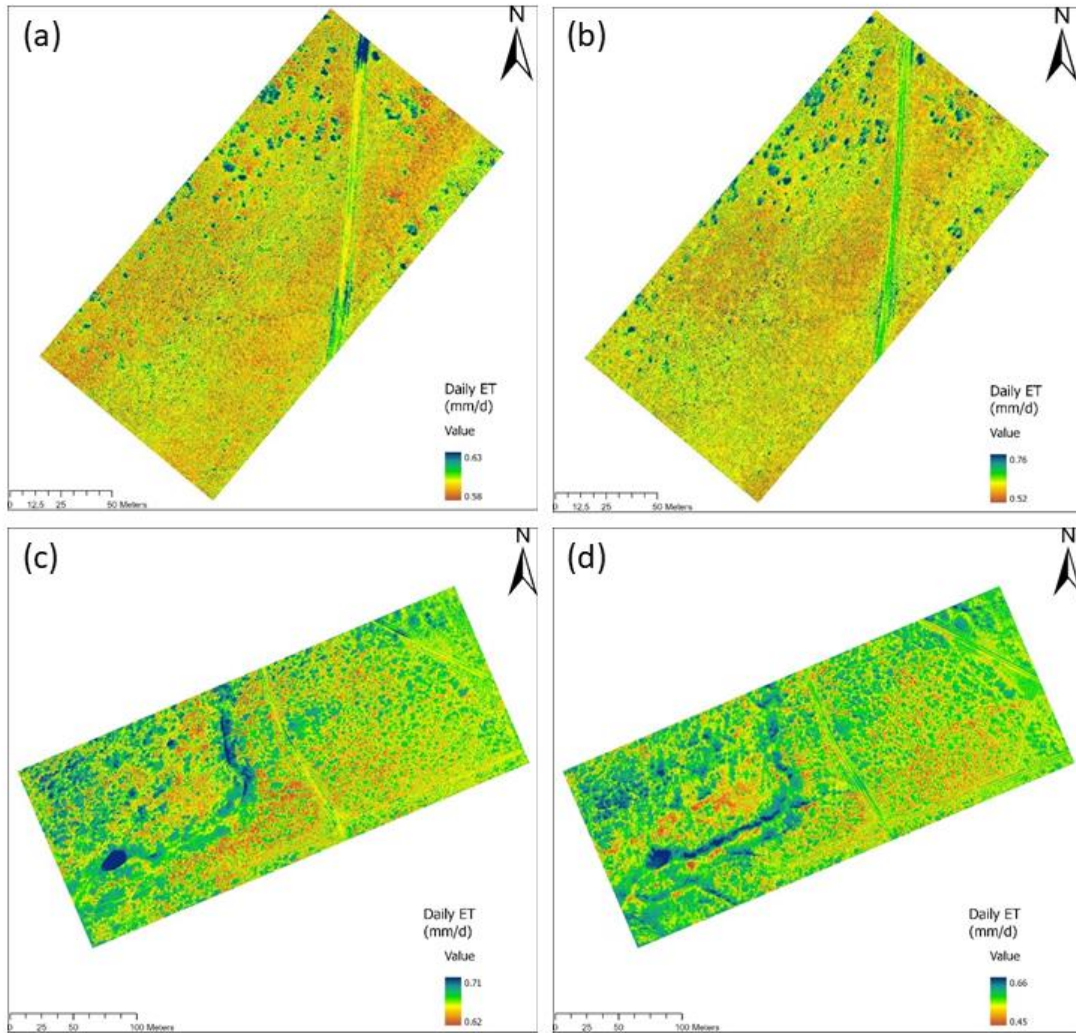
Figure 39 Daily ET maps for the Subshrub area on (a) 04/03/2022, (b) 10/04/2022 and for the Lignum area on (c) 04/03/2022, and (d) 07/05/2022. The colour legends have different ranges.

3.6.3 Monthly ET mapping

Figure 40 shows examples of monthly ET maps for the RRG understorey, Subshrub, and Lignum areas. Large spatial variation is observed at the RRG understorey. The monthly ET varies in a small range for both the Subshrub and Lignum sites. At the Subshrub area, some large shrubs and the road are distinctive on the ET maps. At the lignum site, the channel and road are clearly observed on the map.
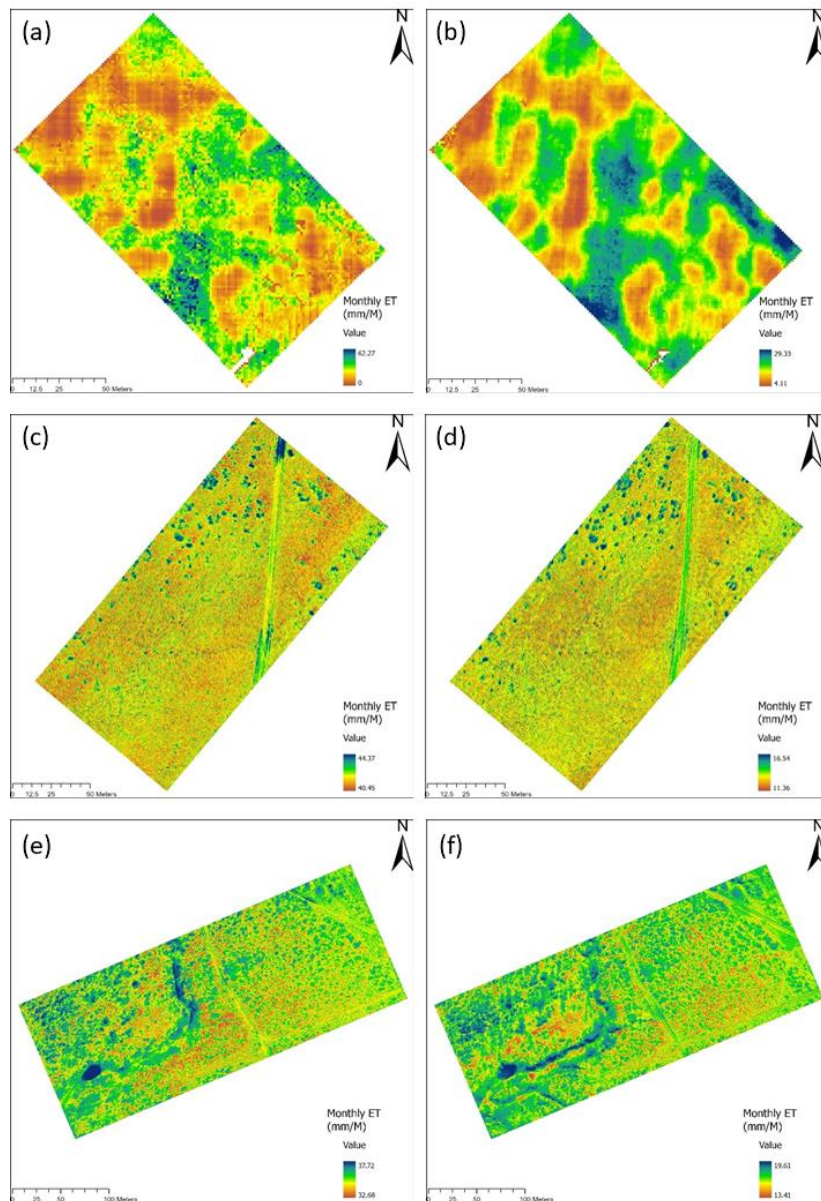
Figure 40 Monthly ET maps of the RRG understorey for (a) March 2022 (b) May 2022, of the Subshrub area for (c) March 2022 (d) April 2022, and of the Lignum area for (e) March 2022 and (f) May 2022. The colour legends have different ranges.

3.6.4 A summary of thermal imagery captures and monthly ET maps

Drone thermal imagery was captured in eleven individual days over the three areas during the whole project period: Lignum 56.7 Ha, Subshrub 24.6 Ha, Understorey 18.6 Ha (Table 4). In three of those days, the surveys were conducted at two times, one in the morning and the other in the afternoon.

Table 4 Thermal imagery acquisition time and data quality.

Date	Lignum	Data quality	Subshrub	Data quality	RRG	Data quality
04/03/2022	10:00-10:30	○	10:52-11:13	☁	11:22-12:16	○
	14:18-14.49	☁	14:12-14:33	○	14:44-15:37	○
10/04/2022		×	11:15-11:36	○	10:03-11:08	○
07/05/2022	12:04-12:35	○	10:30-10:51	○	11:01-11:53	○
	16:28-16:59	○	15:50-16:12	○	14:53-15:44	○
25/06/2022	08:42-09:14	☁	10:38-10:59	○	09:37-10:29	○
	14:28-14:59	☁	15:13-15:35	☁	15:39-16:33	☁
27/05/2023	13:35-14:14	☁	15:53-16:13	☁		×
26/07/2023	16:27-16:51	Incomplete		×		×
13/09/2023	11:24-11:59	○	12:36-12:57	○	12:07-12:31	○
18/10/2023	10:29-11:04	○	11:43-12:03	○	11:12-11:37	-
16/11/2023	11:12-11:48	-	12:24-12:43	-	11:55-12:19	-
17/11/2023	10:49-11:25	-	11:31-11:50	-	12:16-12:40	-

○ good quality ☁ cloud contamination × no data   - No shortwave radiation data

For those thermal surveys of good quality, monthly ET maps have been generated (Table 5). These maps are included in a geodatabase, together with the processed thermal imagery. Overall monthly ET in the Subshrub area has the lowest spatial variability, followed by the Lignum area. ET of the RRG understorey has a large spatial variability. For the Subshrub area, the average monthly mapped ET is similar to station-based monthly ET except for March and June 2022. For the Lignum area, the station-based monthly ET falls within 20% of the average mapped monthly ET. For these two areas of short vegetation, it is very likely that ET can be estimated reasonably well based on one MEP station. For the RRG understorey, monthly ET differs significantly between mapped average and the MEP station. ET mapping becomes important for woodland understorey. Estimation based on one MEP station may not be appropriate because of a large spatial variability in understorey ET.

Table 5 Comparison of monthly total ET and standard deviation for three areas.

Station	Month	Surface	Station estimated ET (mm/month)	Mean ET (mm/month)	Standard deviation (mm/month)
Lignum	Mar 2022	-	42.07	35.27	0.62
	May 2022	-	20.70	17.41	0.65
	Sep 2023	-	56.53	53.18	5.56
	Oct 2023	-	71.09	67.71	6.11
Subshrub	Mar 2022	-	32.16	41.85	0.41
	Apr 2022	-	15.82	13.45	0.60
	May 2022	-	9.92	10.57	0.81
	Jun 2022	-	6.40	15.37	0.37
	Sep 2023	-	25.69	21.59	2.60
	Oct 2023	-	32.13	30.34	3.98
RRG	Mar 2022	All data		24.65	8.45
		Understorey	23.91	22.44	7.51
		Open area		29.96	8.23
	Apr 2022	All data		17.79	6.21
		Understorey	12.82	15.71	5.43
		Open area		22.81	5.01
	May 2022	All data		14.78	4.62
		Understorey	6.84	13.06	3.86
		Open area		18.93	3.56
	Jun 2022	All data		8.44	2.12
		Understorey	2.69	7.79	1.85
		Open area		10.02	1.91
	Sep 2023	All data		14.41	3.22
		Understorey	16.78	13.69	2.88
		Open area		16.15	3.35

In addition, the ET maps based on one instantaneous imaging may be problematic if at the drone survey time, the net radiation measurement point happens to be in shade, e.g., a few hours around noon in September (Figure 41). This is because not everywhere in the understorey is in the shade at the same time. This problem can be solved by replacing the measured net radiation of the problematic time intervals with an estimated net radiation, e.g., by the DST modelling, or the empirical relationship between the above-canopy downwelling shortwave radiation and the net radiation. In this project, the second method was applied.
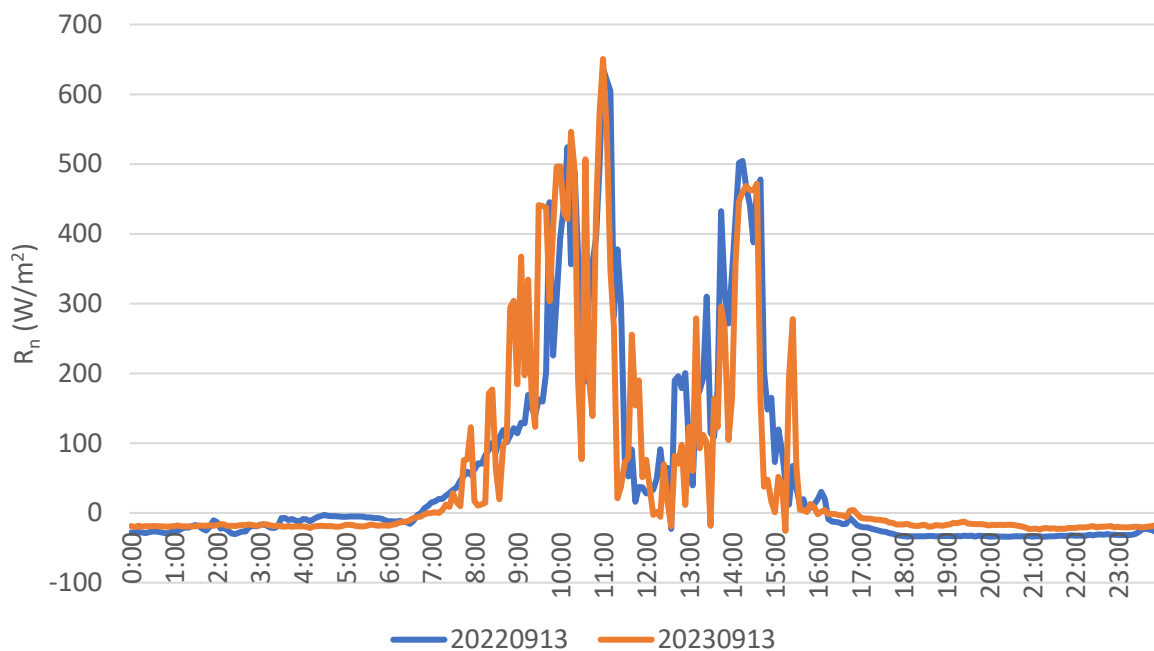
Figure 41 Five-minute interval net radiation measured at the RRG understorey site in two days of one year apart, showing the persistent shadow effect for about two hours around noon.

3.7 Spatial and temporal variabilities of ET in the understorey and short vegetation areas

Of the three studied surfaces, ET in the RRG understorey shows the largest spatial variability. This is most likely due to that the woodland overstorey increases net radiation spatial variability at the understorey surface. This pattern indicates that one MEP station in the understorey is very likely not sufficient for estimating spatially average understorey ET. This notion is supported by significant under-estimated ET based on the station referenced to the average mapped ET (Table 5). In addition, it suggests that ET mapping appears to be more essential for woodland understorey than short vegetation areas. For the

RRG woodland understorey, the average daily ET is 0.52 mm/day (190 mm/y) based on the station data. Actual spatially average ET is likely underestimated by the station. We found the difference between the mapped average and the station estimation for the RRG understorey primarily occurred from April to August where solar elevation was low. During this period, the result based on the station data underestimated mapped average ET by 4.97 mm in April 2022, 7.94 mm in May 2022, 5.75 mm in June 2022, 3.84 mm (interpolated) in July 2022, and 1.95 mm (interpolated) in August 2022. After these underestimations are corrected, the annual ET of the RRG understorey from November 2021 to October 2022 is estimated to be 214 mm. The 2022-2023 River Murray flooding did not significantly change the ET pattern after the flood receded, suggesting that the understorey herbaceous plants do not have a deep root zone. The understorey also shows some ET seasonality, with high ET occurring in summer, and low ET occurring in winter.

ET of the Subshrub and Lignum areas have smaller spatial variations than the woodland understorey. For these two surfaces, one MEP station for each area should provide reasonable estimates of spatial average ET for the surface. At the Lignum area, the station-based ET estimation is about 1 mm/day (or 365 mm/y) for the year before the 2022-2023 River Murray flood. The flood has significantly increased ET for this area till the end of the monitoring period for this site (November 2023), suggesting that the Lignum root zone has stored water from the flood. Of the three sites, the inundation duration was also longest in this area, providing more time for water to infiltrate into the soil. The long inundation duration killed most of the matured Lignum shrubs. At the Subshrub area, the station-based ET estimation is 0.79 mm/day (or 288 mm/y) for the year before the flood. The flood's impact on ET lasted at most for six months following the flood recession.

3.8 Not all thermal images are equally useful

It was found that some images collected were not useful (Table 4). The problem mainly came from unstable sky conditions when the thermal images were undertaken. We used a drone which was shared by multiple users in Flinders University. This means that the drone would not be necessarily available when the sky is clear. This problem can be solved if the project has a designated drone. Although a method has been adopted to correct some images taken under unstable sky conditions, the ones with too dynamic sky conditions are difficult to be adjusted.

We also find that the thermal images around noon and early afternoon are most useful. At this time, solar energy input to the land surface is high, often corresponding to high ET (if water is not in shortage) or high vegetation water stress (if the root zone is short of moisture).

If thermal imaging time is limited, woodland understorey should be listed as the priority. This is because spatial variability in understorey ET is larger than that of short vegetation areas.

4 Conclusions

This report summarises the field instrumentation at three understorey/short-vegetation areas, data collection from spring 2021 to spring 2023, drone surveys, MEP ET modelling, MEP-based mapping methods for instantaneous, daily, and monthly ET.

It is demonstrated that the MEP Evaporation and Transpiration models provide more reliable estimation of hourly ET than the Bowen ratio energy balance method. This is based on the modelling results from the Lignum site and the Subshrub site where data are available for both methods. To map instantaneous ET based on the MEP method, this project adopted the DST radiation model for net radiation mapping, developed an empirical method for surface specific humidity mapping based on ambient weather and local radiative temperature, and developed a method to retrieve understorey surface temperature which is blocked in the thermal images by the overstorey canopy, and derived a site-specific relationship to map RRG leaf area index based on LiDAR data. We also developed the uniform ET ratio method to upscale instantaneous ET maps to daily and monthly ET maps.

The results indicate that the RRG understorey on average lost 214 mm for one year (November 2021-October 2022), while the Subshrub surface lost 288 mm, and the Lignum surface lost 365 mm. Over the same period, the floodplain received 312 mm rainfall. These results imply that for those different land covers (RRG, Subshrub and Lignum), it may lose 2.14, 2.88, and 3.65 ML of water per hectare in a year, solely due to evapotranspiration from understorey and short-vegetation surfaces.

Analysis of post-flood data reveals distinct ET responses among sites. The Lignum site experienced a significant increase in ET, peaking at 40% higher than the previous year, likely due to regrowth after the flood. The Subshrub site's ET rates also increased, reaching a peak in July, influenced by increased soil moisture from rainfall and the recent flood. At the RRG understorey, the flood didn't cause observable ET

changes, likely due to sandy soil texture and a shallow herbaceous understorey root zone. These findings suggest varying responses of different floodplain ecosystems to flooding events.

The ET mapping result suggests that the RRG understorey has a larger spatial variability of ET than the Subshrub and Lignum areas. One MEP station is not sufficient to obtain representative ET estimation for the whole understorey. We recommend use of the spatial modelling methods developed in this project, aided with an ambient weather station, regular drone thermal surveys, once per season LiDAR survey, and distributed relative humidity and temperature monitoring points.

References

Balandier, P., Gobin, R., Precosto, B., Korboulewsky, N. (2022), The contribution of understorey vegetation to ecosystem evapotranspiration in boreal and temperate forests: a literature review and analysis, *European Journal of Forest Research*, 141, 979-997. doi: 10.1007/s10342-022-01505-0.

Gutierrez-Jurado, H., H. D. Guan, J. Wang, H. L. Wang, R. L. Bras, and C. T. Simmons (2015), Maximum entropy production modeling of evapotranspiration partitioning on heterogeneous terrain and canopy cover: advantages and limitations., in *American Geophysical Union Fall Meeting*, edited, American Geophysical Union, San Francisco, USA.

Hajji, I., D. F. Nadeau, B. Music, F. Anctil, and J. F. Wang (2018), Application of the maximum entropy production model of evapotranspiration over partially vegetated water-limited land surfaces, *Journal of Hydrometeorology*, *19*(6), 989-1005. doi:10.1175/jhm-d-17-0133.1.

Heilman, J. L., C. L. Brittin, and C. M. U. Neale (1989), Fetch requiements for Bowe-ratio measurements of latent and sensible heat fluxes, *Agricultural and Forest Meteorology*, *44*(3-4), 261-273. doi:10.1016/0168-1923(89)90021-x.

Lamaud, E., J. Ogee, Y. Brunet, and P. Berbigier (2001), Validation of eddy flux measurements above the understorey of a pine forest, *Agricultural and Forest Meteorology*, *106*(3), 187-203. doi:10.1016/s0168-1923(00)00215-x.

Liu, N., Z. J. Deng, H. L. Wang, Z. D. Luo, H. A. Gutierrez-Jurado, X. G. He, and H. D. Guan (2020), Thermal remote sensing of plant water stress in natural ecosystems, *Forest Ecology and Management*, *476*. doi:10.1016/j.foreco.2020.118433.

Liu, N., H. D. Guan, Z. D. Luo, C. C. Zhang, H. L. Wang, and X. P. Zhang (2017), Examination of a coupled supply-and demand-induced stress function for root water uptake modeling, *Hydrology Research*, *48*(1), 66-76. doi:10.2166/nh.2016.173.

Liu, W. J., H. D. Guan, H. A. Gutierrez-Jurado, E. W. Banks, X. G. He, and X. P. Zhang (2022), Modelling quasi-three-dimensional distribution of solar irradiance on complex terrain, *Environmental Modelling & Software*, *149*. doi:10.1016/j.envsoft.2021.105293.

Payero, J. O., C. M. U. Neale, J. L. Wright, and R. G. Allen (2003), Guidelines for validating Bowen ratio data, *Transactions of the ASAE*, *46*(4), 1051-1060.

Perez, P., F. Castellvi, M. Ibanez, and J. Rosell (1999), Assessment of reliability of Bowen ratio method for partitioning fluxes, *Agricultural and Forest Meteorology*, *97*(3), 141-150.

Tanner, B. D., Greene, J. P., & Bingham, G. E. (1987). A Bowen ratio design for long term measurements. *American Society of Agricultural Engineers (Microfiche collection)(USA)*.

Wang, J., and R. L. Bras (2009), A model of surface heat fluxes based on the theory of maximum entropy production, *Water Resources Research*, *45*, 15. doi:10.1029/2009wr007900.

Wang, J. F., and R. L. Bras (2011), A model of evapotranspiration based on the theory of maximum entropy production, *Water Resources Research*, *47*, 10. doi:10.1029/2010wr009392.

Wang, Y., and H. L. Fang (2020), Estimation of LAI with the LiDAR Technology: A Review, *Remote Sensing*, *12*(20). doi:10.3390/rs12203457.

Yang, Y. T., H. D. Guan, J. L. Hutson, H. L. Wang, C. Ewenz, S. H. Shang, and C. T. Simmons (2013), Examination and parameterisation of the root water uptake model from stem water potential and sap flow measurements, *Hydrological Processes*, *27*(20), 2857-2863. doi:10.1002/hyp.9406.